



ELSEVIER

Nuclear Instruments and Methods in Physics Research B 184 (2001) 255–294

---

**NIM B**  
Beam Interactions  
with Materials & Atoms

---

[www.elsevier.com/locate/nimb](http://www.elsevier.com/locate/nimb)

# Space radiation dosimetry in low-Earth orbit and beyond

E.R. Benton <sup>a,\*</sup>, E.V. Benton <sup>b</sup>

<sup>a</sup> *Eril Research, Inc., P.O. Box 150788, San Rafael, CA 94915-0788, USA*

<sup>b</sup> *Physics Department, University of San Francisco, San Francisco, CA 94117-1080, USA*

Received 2 March 2001; received in revised form 15 June 2001

---

## Abstract

Space radiation dosimetry presents one of the greatest challenges in the discipline of radiation protection. This is a result of both the highly complex nature of the radiation fields encountered in low-Earth orbit (LEO) and interplanetary space and of the constraints imposed by spaceflight on instrument design. This paper reviews the sources and composition of the space radiation environment in LEO as well as beyond the Earth's magnetosphere. A review of much of the dosimetric data that have been gathered over the last four decades of human space flight is presented. The different factors affecting the radiation exposures of astronauts and cosmonauts aboard the International Space Station (ISS) are emphasized. Measurements made aboard the Mir Orbital Station have highlighted the importance of both secondary particle production within the structure of spacecraft and the effect of shielding on both crew dose and dose equivalent. Roughly half the dose on ISS is expected to come from trapped protons and half from galactic cosmic rays (GCRs). The dearth of neutron measurements aboard LEO spacecraft and the difficulty inherent in making such measurements have led to large uncertainties in estimates of the neutron contribution to total dose equivalent. Except for a limited number of measurements made aboard the Apollo lunar missions, no crew dosimetry has been conducted beyond the Earth's magnetosphere. At the present time we are forced to rely on model-based estimates of crew dose and dose equivalent when planning for interplanetary missions, such as a mission to Mars. While space crews in LEO are unlikely to exceed the exposure limits recommended by such groups as the NCRP, dose equivalents of the same order as the recommended limits are likely over the course of a human mission to Mars. © 2001 Elsevier Science B.V. All rights reserved.

---

## 1. Introduction

The accurate measurement of astronaut and cosmonaut exposure to ionizing radiation during spaceflight may well represent the single most difficult challenge in radiation dosimetry. The radiation environment in space is typified by a wide

variety of primary particles covering an extended range of energies. When passing through the mass of a spacecraft and its contents, these particles can participate in a number of different types of nuclear interaction, producing a complex complement of both charged and neutral secondary particles. While the number of different particle species is large and the energy spectrum which they occupy is quite broad, their fluxes are often low. Relatively rare events associated with solar flares and coronal mass ejections (CMEs) can produce

---

\* Corresponding author.

E-mail address: [eric@erilresearch.com](mailto:eric@erilresearch.com) (E.R. Benton).

sudden and dramatic increases in flux. Thus the instrumentation required to measure the radiation field aboard spacecraft must be both extremely sensitive and robust. The constraints imposed by spaceflight often mean that ordinary, off-the-shelf dosimeters cannot be used and specialized instrumentation and techniques must be developed. This paper will address a number of issues involved in conducting effective space radiation dosimetry and will review much of the relevant data collected over the past four decades in the effort to meet this challenge.

The emphasis of this paper is on space radiation dosimetry as it pertains to crew health and safety. First the sources of ionizing radiation in low-Earth orbit (LEO) and in interplanetary space are described, as is the production of secondary particles resulting from interactions between primary charged particles and the mass of a spacecraft and its contents. A section on space dosimetry methods describes both passive and active instrumentation routinely used aboard piloted spacecraft for crew and area dosimetry. The next section reviews dose measurements carried out aboard both US and Russian spacecraft since the inception of human spaceflight, including data obtained over the history of the Russian Mir Orbital Station and from the US Space Shuttle Program. A survey of the radiation environment aboard LEO spacecraft emphasizes the dependence of dose and dose-equivalent rates on spacecraft shielding and orientation and on orbital altitude and inclination. In addition, we review the small amount of extant neutron dosimetry data measured aboard piloted spacecraft and dosimetry measurements made external to spacecraft. A section on the radiation exposure of crews on missions outside the Earth's magnetosphere presents some estimates of dose equivalent for human missions to Mars. A section on radiation exposure limits for space crews that includes the latest recommendations of the National Council on Radiation Protection and Measurement (NCRP) follows. Although intimately related to the topic of crew dosimetry, this paper will not discuss space radiation dosimetry as it pertains to radiation-sensitive electronics and materials. Also this paper will not address issues of ionizing radiation effects on tissue at a cellular or

molecular level. Finally we will conclude by summarizing where space radiation dosimetry is today and assessing what still remains to be done in the area of radiation dosimetry for the International Space Station (ISS) and for interplanetary spaceflight.

## **2. Sources of ionizing radiation**

Astronauts and cosmonauts aboard LEO spacecraft such as the NASA Space Shuttle and ISS or aboard spacecraft traveling outside the Earth's magnetosphere on missions to and from the Moon or Mars are exposed to levels of ionizing radiation far in excess of those encountered on the ground. Shown in Fig. 1 are the three principal sources of primary ionizing radiation in LEO: (1) galactic cosmic rays (GCRs) are charged particles that originate from beyond the solar system; (2) energetic electrons and protons are trapped in the geomagnetic field and make up the Earth's radiation belts (ERBs) and (3) solar particle events (SPEs) are high fluxes of charged particles encountered during rare but intense solar flares and CMEs. In LEO, a fourth source, albedo neutrons and protons, is sometimes also mentioned. These are secondary particles, produced in interactions between GCRs and the Earth's atmosphere, with trajectories that take them back up into space. The albedo component is small and of low energy and as such is usually not considered a significant source of astronaut radiation exposure.

Each of the three major sources, summarized in Table 1, makes a contribution to the primary radiation flux encountered by an LEO spacecraft. The relative size, energy and charge distribution of each component are dependent on a large number of parameters including the altitude and inclination of the spacecraft's orbit, the orientation of the spacecraft relative to the Earth and Sun and the particular phase of the 11-year solar cycle. Trapped radiation, of course, is not found in interplanetary space, but the fluxes GCRs and SPEs encountered in interplanetary space are more intense due to lack of protection afforded by the geomagnetic field.

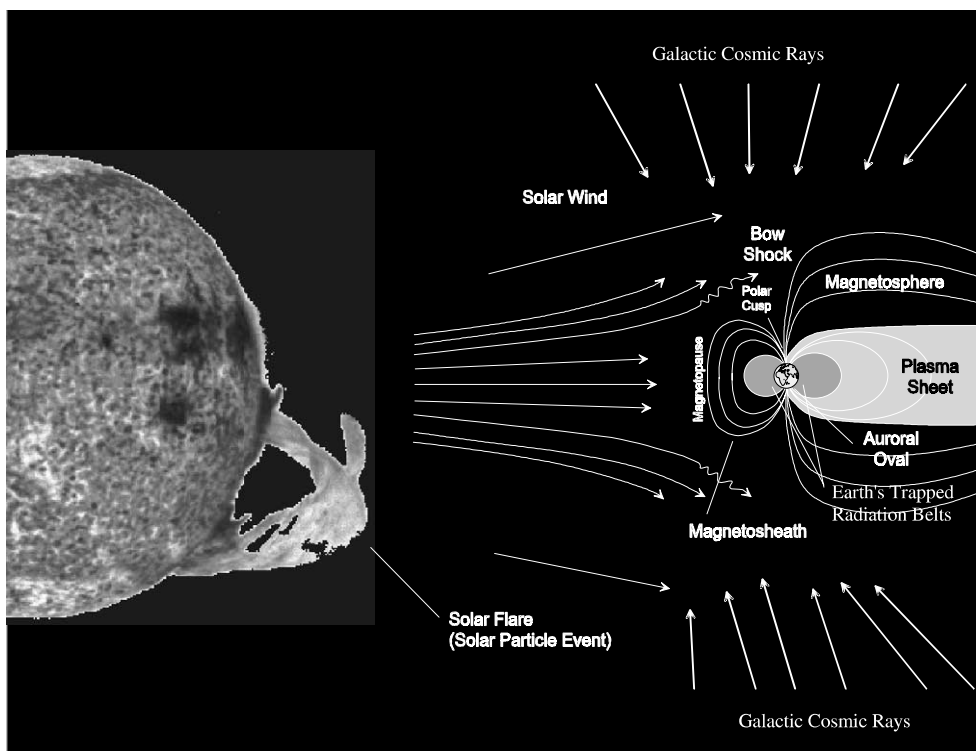


Fig. 1. The three principal sources of space radiation: (1) galactic cosmic rays, (2) trapped radiation in the ERBs and (3) solar particle events. All three sources are affected by the Earth's magnetic field.

While passing through the skin and structure of a spacecraft, primary particles can undergo nuclear interactions with nuclei that constitute the spacecraft's mass, producing a wide variety of secondary particles. The radiation environment in the interior volume of a spacecraft is thus greatly modified from the one encountered in empty space.

### 2.1. Galactic cosmic rays

Galactic cosmic rays are charged particles that originate from sources beyond our solar system. The distribution of GCRs is believed to be isotropic throughout interstellar space. The energies of GCR particles range from several tens up to  $10^{12}$  MeV and, within the solar system, the GCR spectrum is peaked around 1 GeV. The GCR spectrum consists of 98% protons and heavier ions (baryon component) and 2% electrons and positrons (lepton component). The baryon component

is composed of 87% protons, 12% helium ions (alpha particles) and the remaining 1% heavy ions of charge 3 (Li)–92 (U). Fig. 2 shows the relative abundances of GCRs [1]. Highly energetic particles in the heavy ion component, typically referred to as HZE particles, play a particularly important role in space dosimetry. HZE particles, especially iron nuclei which are relatively plentiful compared to the other high  $Z$  ions, possess high-LET and are highly penetrating, giving them a large potential for radiobiological damage.

Often included with the GCRs is the anomalous cosmic ray component. Anomalous cosmic rays are low-energy charged particles that are only partially ionized. Because of their low energy, these particles are seldom able to penetrate into the habitable volume of a spacecraft or produce much in the way of biological damage and are therefore not considered terribly important from a crew dosimetry point of view.

Table 1  
The space radiation environment in LEO and in interplanetary space

	Galactic cosmic rays	Earth's radiation belts	Solar particle events
Primary composition	<p>98% hadrons <math>\left\{ \begin{array}{l} 87\% \text{ protons} \\ 12\% \alpha\text{-particles} \\ 1\% \text{ heavy ions} \end{array} \right.</math></p> <p>2% leptons (electrons and positrons)</p>	<ul style="list-style-type: none"> <li>• Electrons &lt;6 MeV</li> <li>• Protons &lt;250 MeV</li> </ul>	<ul style="list-style-type: none"> <li>• Mostly low-energy protons &amp; electrons</li> <li>• Rarely higher-energy protons</li> <li>• Some heavy ions</li> </ul>
Effect of solar cycle	<ul style="list-style-type: none"> <li>• Flux inversely proportional to solar cycle</li> <li>• Solar modulation affects <math>\leq 1</math> GeV/n component</li> </ul>	<ul style="list-style-type: none"> <li>• Solar cycle affects atmospheric scale height and east/west proton anisotropy</li> <li>• Creation of temporary belts during solar max</li> </ul>	<p>Frequency and magnitude of SPE proportional to solar cycle</p> <ul style="list-style-type: none"> <li>• High probability at solar max</li> <li>• Low probability at solar min</li> </ul>
Effect of geomagnetic field	<p>Protection in LEO due to cutoff</p> <p>Rigidity, function of geomagnetic latitude</p>	<ul style="list-style-type: none"> <li>• Raison d'être</li> <li>• South Atlantic Anomaly</li> </ul>	<p>Protection in LEO due to cutoff</p> <p>Rigidity, function of geomagnetic latitude</p>
Effect of spacecraft shielding	<ul style="list-style-type: none"> <li>• Little attenuation through ionization</li> <li>• Projectile and Target Fragmentation by heavy ions</li> <li>• Target fragmentation by protons</li> </ul>	<ul style="list-style-type: none"> <li>• Electrons fully attenuated, some production of Bremsstrahlung</li> <li>• Attenuation of low-energy protons</li> <li>• Target fragmentation by higher-energy protons</li> </ul>	<ul style="list-style-type: none"> <li>• Low-energy protons attenuated</li> <li>• Higher-energy protons and heavy ions can undergo nuclear interactions</li> </ul>
Models/predictive capability	<p>Good agreement with measurements</p> <ul style="list-style-type: none"> <li>• Badhwar/O'Neill</li> <li>• CREME96 (Nymmik)</li> </ul>	<p>Electrons: AE-8 (empirical model, old dataset, some refinements)</p> <p>Protons: AP-8 (empirical model, old dataset, some refinements) underpredicts at solar max overpredicts at solar min</p>	<p>Little predictive capability</p> <ul style="list-style-type: none"> <li>• NOAA Space Environment Center</li> <li>• GOES satellites</li> <li>• Neutron ground monitors</li> </ul>
Relative contribution in LEO	<ul style="list-style-type: none"> <li>• Dominates for high-inclination orbits</li> <li>• <math>\sim 50\%</math> of ISS dose</li> </ul> <p>In LEO, relative contributions from all sources are dependent on orbital parameters (orbital inclination, altitude), spacecraft orientation, solar cycle and temporal variations in the geomagnetic field in a highly complex way.</p>	<ul style="list-style-type: none"> <li>• Dominates for low-inclination, high-altitude orbits</li> <li>• <math>\sim 50\%</math> of ISS dose</li> </ul>	<ul style="list-style-type: none"> <li>• More severe in higher-inclination orbits</li> <li>• Unknown contribution to ISS Dose</li> </ul>
Relative contribution in free space	<p>Omnipresent</p> <p>In free space, relative contributions dependent on solar modulation and spacecraft shielding</p>	<p>N/A</p>	<p>Presents potentially large risk, especially during solar maximum</p> <p>spacecraft shielding</p>

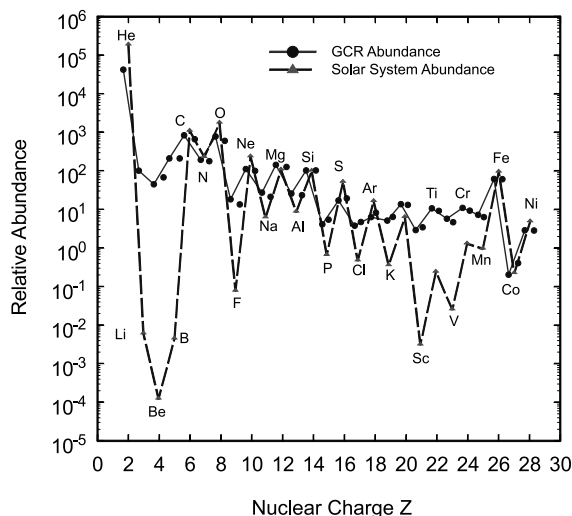


Fig. 2. Abundance of GCR from He to Ni. Also shown are solar system abundances for these same elements [1]. Abundances of nuclei of  $Z$  greater than Ni fall well below the scale of this plot.

The flux of GCRs with energy below about 1 GeV is affected by the sun's 11-year cycle as shown in Fig. 3 [2]. The GCR flux entering the solar system interacts with the solar wind and is partially attenuated. This attenuation is greatest during solar maximum when the solar wind is most intense. Conversely, GCR flux is greatest during

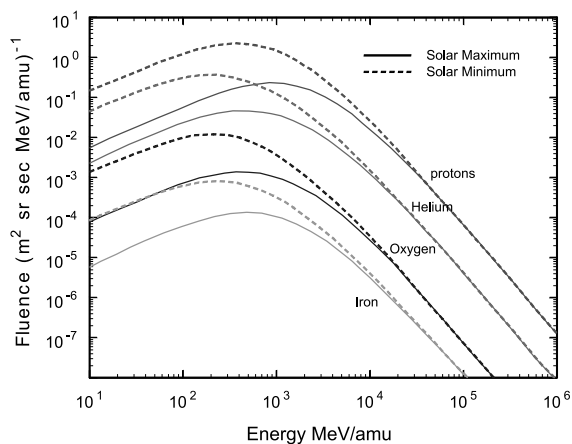


Fig. 3. Solar cycle effect on the GCR energy spectrum for hydrogen, helium, oxygen and iron. Increased intensity of the solar wind associated with solar maximum attenuates the GCR spectrum below  $\sim 1$  GeV/amu [2].

solar minimum when the decreased solar wind produces less attenuation. The dependence of GCR flux on solar cycle has important implications (vide infra) for long duration space travel to Mars and the outer solar system.

GCR, being composed of charged particles, is also affected by the Earth's magnetic field. Charged particles tend to follow the lines of the geomagnetic field. Since the geomagnetic field lines are parallel to the Earth's surface near the equator, all but the most energetic particles are deflected away by this geomagnetic cutoff. The geomagnetic field over the north and south poles points toward the Earth's surface and, at high latitudes, GCR particles are funneled toward the poles. A LEO spacecraft receives its greatest exposure to GCR while near the poles and a minimum of GCR exposure while near the equator. In fact, low-inclination orbits such as the  $28.5^\circ$  orbit of the Hubble Space Telescope and many early Space Shuttle missions are exposed only to the highest-energy GCR.

Several models of the GCR flux have been developed over the last several decades. The early CREME model of Adams [3] has been largely superseded by a number of newer models including the Badhwar and O'Neill model [4] and the Nymmik model [5]. These new models are based on the diffusion/convection theory of solar modulation, wherein solar modulation is characterized by a deceleration potential determined from ground-based neutron monitor data. The Nymmik model has been incorporated into the CREME96 program and is available for use directly over the Internet [6].

## 2.2. Earth's trapped radiation belts

The Earth is surrounded by intense regions of energetic protons and electrons referred to as the Van Allen Belts or the Earth's trapped radiation belts (ERBs). These particles are trapped by the geomagnetic field where they follow a complex motion, illustrated in Fig. 4. The charged particles revolve around a geomagnetic field line in what is called cyclotron motion. Because the geomagnetic field is roughly equivalent to that of a dipole, it is not uniform and the field lines converge near the poles. This causes the charged particles to move

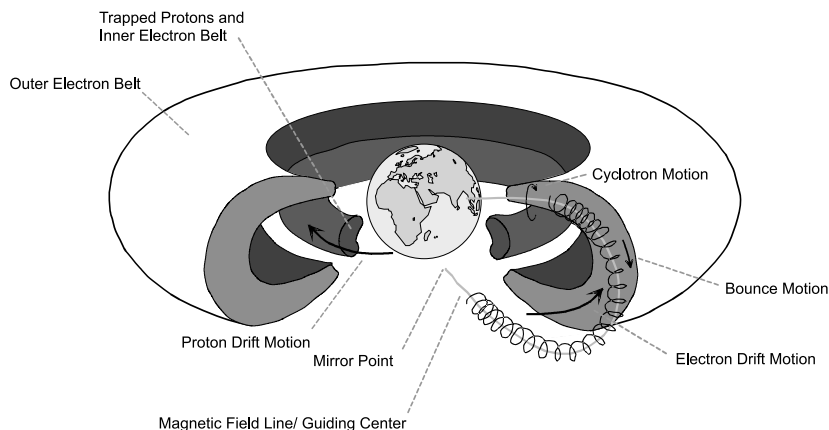


Fig. 4. The ERBs: charged particles undergo three types of motion: cyclotron motion around a geomagnetic field line, bounce motion along the field line and drift motion around the Earth.

back and forth along the field lines, reversing their directions at mirror points near the poles. Finally there is a drift of the protons to the west and of the electrons to the east.

Trapped electrons occur in two belts or zones. The first, inner zone extends to about 2.4 Earth radii ( $R_E$ ) and consists mostly of electrons with energies less than  $\sim 5$  MeV. The second or outer zone extends from about 2.8 to 12  $R_E$  and contains electrons with energies up to about 7 MeV. The gap between the inner and outer electron belts is referred to as the slot region. Electron flux is about an order of magnitude greater in the outer zone than in the inner zone. Since most of the electron flux is of low energy, it is stopped by the shielding provided by the skin of the spacecraft. Most of the flux lies below the energy ( $\sim 10$  MeV) where Bremsstrahlung X-ray production becomes important. This, in addition to the fact that the most intense electron fluxes occur at altitudes well above LEO, means that trapped electrons present little risk to human health.

Trapped protons occur in only a single region that decreases in intensity as a function of distance from the Earth. Trapped protons extend in energy from several to several hundred MeV and form a broad peak between 150 and 250 MeV. The majority of the trapped proton belt lie at altitudes above those traversed by the orbit of the ISS. However, due to the fact that the axis of the

Earth's magnetic field is slightly displaced from its axis of rotation, there is a region off the coast of Brazil called the south Atlantic Anomaly (SAA) where the geomagnetic field drops unusually close to the Earth's surface. In the SAA the trapped proton belt intersects the orbits of low-altitude spacecraft such as the Shuttle and ISS. When the ISS passes through the SAA, it receives its maximum exposure to trapped protons. For the  $51.56^\circ$  inclination,  $\sim 400$  km altitude orbit of the ISS, about half the ionizing radiation dose is from trapped protons in the SAA and half is from GCR at higher latitudes [2].

Models of the ERB are still based primarily on the static AP-8 proton [7] and AE-8 electron [8] flux maps. These data, acquired between 1966 and 1980, have been combined into the RADBELT model available from the National Space Sciences Data Center [9]. There have been a number of efforts to extend these models based on datasets measured by other spacecraft including TIROS and NOAA satellites [10] and the CRRES, SAMPEX and STRV satellites [11]. A useful Internet site for calculating trapped radiation exposure is the SPENVIS website run by Heynderickx [12].

### 2.3. Solar particle events

The third source of ionizing radiation takes the form of energetic particles emitted by the sun

during solar flares and CMEs. These fluxes included electrons, protons and heavier charged particles up to iron. From the space radiation health perspective, we are most concerned with protons due to a combination of their relative abundance and their high energy. Solar particle events are relatively rare and occur most often during the solar maximum phase of the 11-year solar cycle as illustrated in Fig. 5 [13]. Solar particle events have been variously defined as events with total proton fluences  $>30$  MeV of  $10^6$ ,  $3 \times 10^6$  and  $10^7$   $\text{cm}^{-2}$ . The frequency of these events is quite varied, but  $\sim 50$  such events can be expected over the course of a single solar cycle. A major SPE is defined as an event having a proton fluence  $>10$  MeV of  $10^{10}$   $\text{cm}^{-2}$  and one or two

events of such a magnitude can be expected per solar cycle.

There are two types of SPEs: those produced by impulsive flares and those produced by CMEs [14]. These two types of SPEs are illustrated in Fig. 6. SPEs associated with impulsive solar flares are short-lived, usually of the order of hours, and are characterized by relatively large fluxes of electrons. Total fluence is small, between  $10^7$  and  $10^8$   $\text{cm}^{-2}$  and these events are restricted to a  $30$ – $45^\circ$  angle in solar longitude. The second type of SPE, associated with large CMEs, is much longer-lived, of the order of days and is characterized by much larger fluxes of protons. Total fluence can exceed  $10^9$   $\text{cm}^{-2}$  and the event can spread over a broad angle in solar longitude extending from  $60^\circ$  to as much as  $180^\circ$ .

The proton fluence spectra from several of the largest SPEs on record are shown in Fig. 7 [15]. Included in this figure is the large SPE of October 1989. The differential proton flux spectrum as measured by the NOAA Geostationary Observational Environment Satellite (GOES) 7 during the October 1989 series of events is shown in Fig. 8 [16]. The time profile of a typical SPE starts off with a rapid exponential increase in flux, reaching a peak in minutes to hours. Following the peak, there is a gradual decay in flux that lasts of the order of hours to days. A second peak can arise when the interplanetary shock wave produced by the CME passes the Earth. Such a shock enhancement can be seen in the October 1989 GOES-7 data at a time just preceding 21 October. The October 1989 event was actually quite unique, not

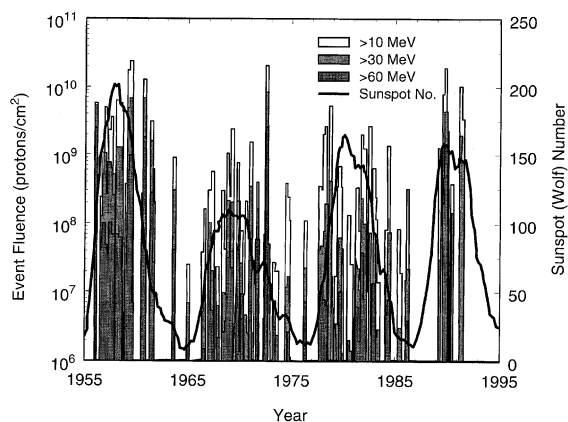


Fig. 5. Major SPEs over the last four solar cycles (adapted from [13]).

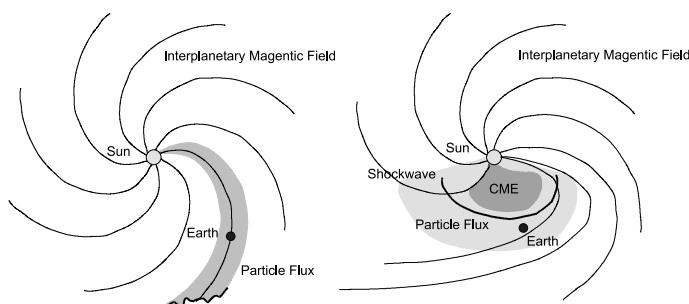


Fig. 6. The two types of SPE: an SPE associated with an impulsive flare (left) and an SPE associated with a CME (right) (adapted from [14]).

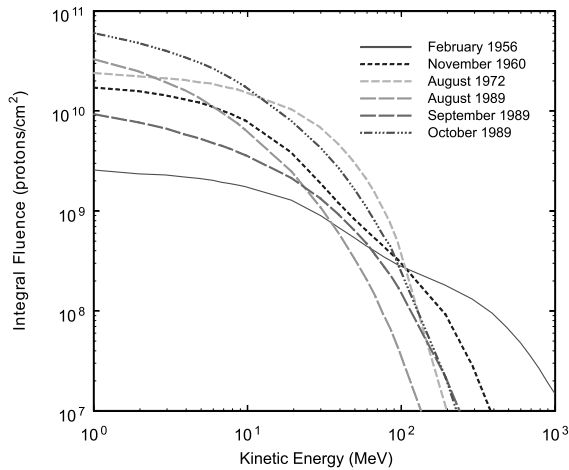


Fig. 7. Integral proton fluences for several major SPEs over the last four solar cycles [15].

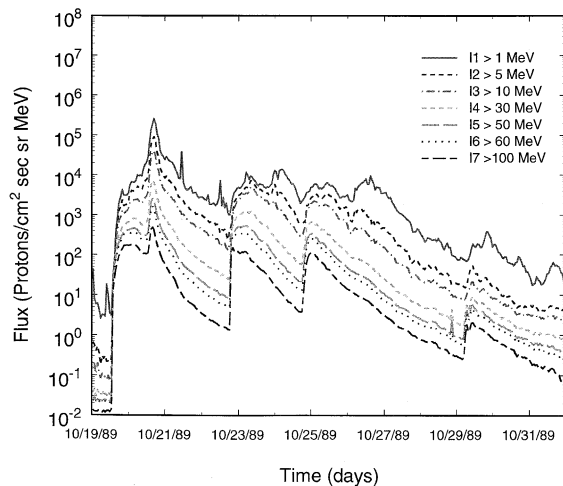


Fig. 8. Differential proton flux from the October 1989 SPE series as measured by the NOAA GOES-7 satellite [16].

only in its overall intensity, but by virtue of the fact that this was actually made up of a long series of SPEs. The magnetic field carried by the SPE shock interacts with the geomagnetic field and thereby lowers the cutoff rigidity. This allows lower-energy particles from the SPE to reach lower latitudes, leading to an overall enhancement of the LEO dose rate.

## 2.4. Secondary particles

Most of the energy loss experienced by primary particles as they pass through a spacecraft takes the form of ionization. However, the energies of many of these particles are sufficiently high and the amount of shielding represented by the spacecraft is sufficiently large that a fraction of these primary particles will undergo nuclear interactions with the constituent nuclei of the spacecraft and its contents, producing secondary particles. The production of secondaries is summarized in Fig. 9.

Two types of nuclear interaction between primary charged particles and target nuclei of the spacecraft are of importance – target fragmentation and projectile fragmentation. Target fragmentation occurs when a high-energy charged primary, typically a trapped or GCR proton, collides with a heavy nucleus such as an Al nucleus of the spacecraft structure or a C or O nucleus of an astronaut's body. Depending on the kinetic energy of the primary charged particle, the nuclear interaction can follow a number of different channels, producing two or more secondary particles. These secondaries can include knockout protons, neutrons and  $\alpha$ -particles, as well as recoil heavy nuclei.

Projectile fragmentation occurs when a HZE particle collides with a target nucleus. Again, depending on the energy and charge of the primary particle and the angle of the collision, a large number of reaction channels are possible. In addition to producing high-energy neutrons and protons, these reactions can also produce larger projectile fragments that retain much of the kinetic energy of the primary HZE particle.

The secondaries produced by target and projectile fragmentation continue to traverse the volume of the spacecraft and may themselves undergo further nuclear reactions. This is especially true in the case of high-energy neutrons. The spacecraft mass can be thought of as a medium in which high-energy charged particles initiate hadronic cascades. In addition,  $\gamma$ -rays and neutral pions produced in these nuclear reactions can initiate electromagnetic cascades. Each of the secondary particles produced in these nuclear interactions possesses some potential to cause biological



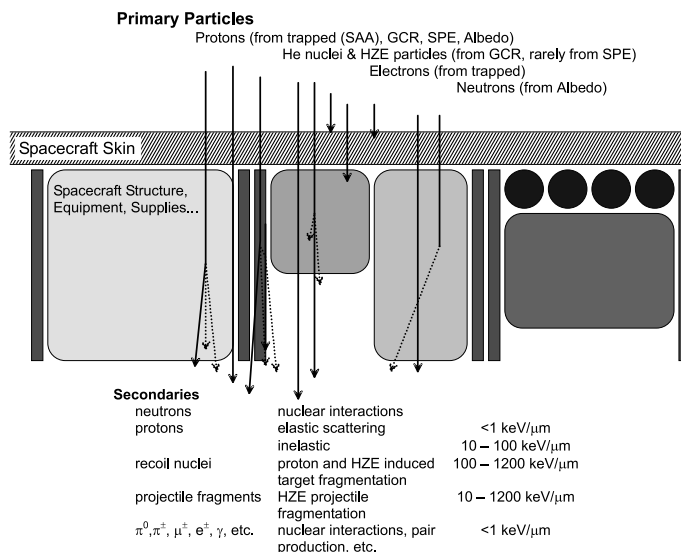


Fig. 9. The transport of primary radiation through the spacecraft structure and contents and the generation of secondaries. The most important secondaries in terms of radiation protection are neutrons and the high-LET target and projectile fragments.

damage should it pass through the body of an astronaut.

The production of secondary neutrons is intimately related to the effect of spacecraft shielding in modifying the primary charged particle flux. The accurate measurement of neutron fluences and their contribution to dose equivalent during spaceflight remain one of the greatest challenges in space radiation dosimetry. Relatively few measurements have been made of neutron flux and its contribution to dose equivalent inside LEO spacecraft. Partly as a result of the scarcity of neutron dosimetry data from space, the relative contribution from neutrons to an astronaut's total radiation exposure is poorly understood. For an ISS type orbit (51.6° inc., ~450 km altitude) estimates of the neutron contribution to an astronaut's total dose equivalent range from 30% to 60% [17,18]. The quality factor of these neutron fluxes tends to be 4–5 times greater than that for charged particles [19].

In LEO, the major source of an astronaut's neutron dose equivalent is from secondary neutrons. A smaller fraction comes from low-energy albedo neutrons from the Earth's atmosphere. At a particular location within a spacecraft, the neutron spectrum depends on the localized shielding

distribution (quantity and elemental composition of the mass distribution) surrounding this location. The neutron spectrum inside spacecraft can be considered to occupy several discrete energy intervals: (1) evaporation neutrons of energy between 1 and about 20 MeV, (2) intranuclear cascade neutrons of energies between 20 and 200 MeV, (3) neutrons from the fragmentation of high-energy GCR ranging in energy from between 500 MeV and 5 GeV and (4) moderated neutrons with energy <1 MeV. It is estimated that neutrons in each of the first three energy regions make a roughly equal contribution to dose equivalent [19].

The production of secondary particles has been modeled by a number of different radiation transport codes. These codes typically take one of the two approaches – analytic or Monte Carlo. Wilson et al. [20] at the NASA Langley Research Center are developing two analytic codes for the transport of space radiation through both tissue and spacecraft shielding materials. The BRYNTRN program models the transport of protons through matter while the HZETRN code is an extension of the BRYNTRN program to heavy ions. Both codes are based on analytically solving the Boltzmann equation in one dimension. The Monte Carlo code most often used for the

transport of space radiation is an adaptation of the HETC code first developed at the Oakridge National Laboratory [18]. HETC lacks the ability to transport heavy ions. Efforts are now underway by Armstrong and Townsend to couple the HETC code with the HZETRN [21]. More recently, Pinsky at University of Houston has been working on adapting the FLUKA Monte Carlo code, developed for high-energy applications at CERN, for use in transporting space radiation [22].

### 3. Space dosimetry methods

The demands and constraints placed on instruments designed to carry out radiation dosimetry aboard piloted spacecraft are far more stringent than those for nearly all ground-based applications as well as for unpiloted satellites and space probes. These constraints are of three basic types. First and foremost is crew safety. The operation of the instrument and its potential failure modes cannot in anyway jeopardize crew health and safety. This applies to obvious things like high-voltage power supplies in active detectors, but also applies in more subtle ways – for example, in the use of glass, the outgassing of polymers, etc.

The second type of constraint has more to do with economics. Because of the high cost of launching equipment and supplies into orbit, instrumentation must be relatively small and of low mass. The instrument should also be of a robust design, able to withstand a large amount of use and abuse without failing, since the on-orbit availability of spare parts is minimal and cost to return an instrument to the ground for repair is prohibitive. In space there is always more demand for electrical power than can be provided by solar arrays so the detector needs to use as little power as possible. This favors passive detectors and, in some circumstances, battery-operated detectors. Similarly, on orbit, there are always a lot more data needing to be transmitted to the ground than there is available bandwidth. This again favors passive detectors and in the case of active detectors, large capacity data storage is often required. The size and mass constraints that apply to personal dosimetry on the ground also apply in space. A crew

personal dosimeter needs to be small enough and light enough that it can be comfortably carried by the astronaut without getting in the way.

The third and possibly most challenging constraint concerns the large dynamic range of sensitivities required of the detectors in terms of particle energy, flux, resolution, etc. Particle fluxes are often quite low – depending on the type of particle, often less than one particle per minute will be registered by the detector. However, in rare situations such as during a large SPE, fluxes can increase by several orders of magnitude. The different sources of primary charged particles combined with the effects of spacecraft shielding in modifying the primary flux lead to a radiation environment inside a spacecraft consisting of many different types of particles and occupying an extremely broad range of energies. The optimal radiation monitoring instrument needs to be sensitive to as much of this environment as possible. It is desirable to have good charge, energy and LET resolution in order to identify the different particles and to assign appropriate values of quality factor. This is especially relevant in the case of neutrons where it is often difficult to discriminate between the charged particle component and the neutron flux. As in all situations, active detectors have the advantage of time resolution over passive detectors.

Differences in dose of up to a factor of 2 have been measured between different locations within the Mir Orbital Station during the same time period, reflecting differences in shielding immediately surrounding the different locations [2]. For fixed oriented spacecraft such as ISS, differences in the directionality of the primary radiation field will also lead to large differences in dose measured throughout the habitable volume. This makes it necessary to conduct personal dosimetry for each astronaut and often makes it desirable to carry out area dosimetry at a number of different locations within the spacecraft. Obviously no one detector can fulfill all the criteria listed above. Spacecraft radiation dosimetry has historically been implemented by a suite of different detectors, each optimized to measure a different radiation component, in such a way that their results can be combined to create a total picture of the space radiation environment.

### 3.1. Passive detectors

The advantages inherent in passive detectors – small size, low mass, safety, relative ease of use and zero power consumption – have made them the detector of choice for much of the history of human spaceflight. Passive detectors have most commonly been used for crew dosimetry and just about every astronaut and cosmonaut who has flown has worn at least one passive dosimeter. Passive detectors used for crew and area dosimetry aboard piloted spacecraft have been mainly of two types: thermoluminescent detectors (TLDs) and solid-state nuclear track detectors (SSNTDs). The type of TLD most widely used is LiF, although other types of TL material have also been employed. Among the disadvantages of TLDs is that they provide no LET information and consequently no information about the dose equivalent. In addition TLDs tend to record the dose for high-LET ( $\geq 10$  keV/ $\mu\text{m}$ ) radiation with less than 100% efficiency and, thus, systematically undermeasure the total dose [23].

In the first decades of human spaceflight, before the development of CR-39 as a track detector, plastic nuclear track detectors (PNTD) such as cellulose nitrate (CN) and Lexan polycarbonate were widely used. The first use of CR-39 PNTD in space coincided with the first flight of the Space Shuttle in 1981 [24] and CR-39 has remained the PNTD of choice ever since. CR-39 PNTD is used to measure the LET spectrum above  $\sim 5$  keV/ $\mu\text{m}$ . Fig. 10 shows a number of LET spectra measured by the group of Benton et al. at the University of San Francisco (USF) over the past three decades. CN possesses a minimum LET threshold of  $\sim 90$  keV/ $\mu\text{m}$  while the minimum LET threshold of Lexan is  $\sim 250$  keV/ $\mu\text{m}$ . Thus only the high-LET end of the spectrum could be measured by PNTDs during the pre-Shuttle era. In addition, the methodology of track detector analysis had not yet progressed to the point where short-range, high-LET secondaries could be efficiently measured. For this reason, early LET spectra measurements in PNTD tend to be significantly lower than those made more recently.

The Benton group at USF has developed a technique for combining absorbed dose measure-

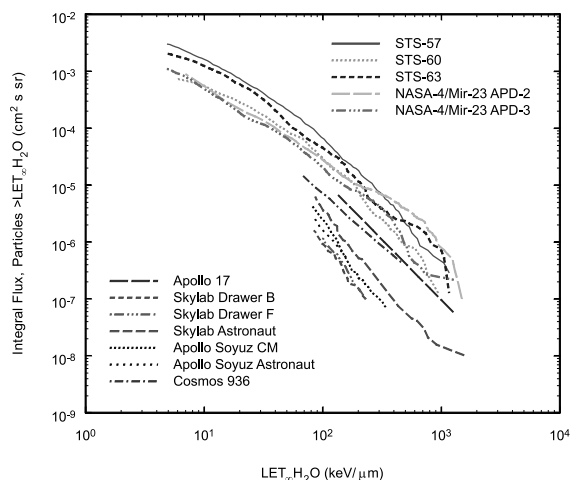


Fig. 10. Integral LET flux spectrum measured by USF using PNTDs for selected space missions over the last 30 years.

ments from TLDs with the LET spectrum measured in CR-39 PNTDs, yielding total dose equivalent. Absorbed dose is measured using TLD-700 while CR-39 PNTDs are used to measure the  $\text{LET}_{\infty} \text{H}_2\text{O}$  spectrum  $\geq 5$  keV/ $\mu\text{m}$ . The high-LET contribution to total dose measured by the PNTDs is subtracted from the TLD absorbed dose with the aid of an empirically determined dose efficiency function [23]. The remaining TLD dose is assumed to have a quality factor of 1 and is combined with the dose and dose equivalent spectra measured by the PNTDs to yield corrected total dose, dose equivalent and mean quality factor. This method has seen widespread application aboard US and Russian spacecraft and recoverable satellites over the last two decades.

A variety of other passive detectors have been used in space for dosimetry purposes, but to a far lesser degree than TLDs or PNTDs. Principle among these are photographic nuclear emulsions. These were widely used during the earliest years of human spaceflight, but have fallen into disuse owing to the labor-intensive effort and careful handling required to analyze them. They are still used on occasion for neutron dosimetry (infra-vide). Other types of passive detectors including bubble detectors, activation foils and fission foils have also been used in space, again mainly for neutron dosimetry, with mixed success, owing

mainly to the highly complex nature of the radiation field aboard spacecraft.

The principal disadvantage of passive detectors is their inability to provide real-time or time-resolved data. Passive detectors, especially PNTDs, are labor-intensive to analyze, and processing and analysis must be carried out on the ground. The Pille TLD System, developed by the KFKI Atomic Energy Institute, Budapest, overcomes a number of these limitations [25]. The Pille System permits TLDs to be read out, annealed and re-used on orbit. In one form or another the Pille system has been in use aboard Russian spacecraft since the Salyut-7 Orbital Station missions and a new version was recently installed aboard the ISS.

Despite their disadvantages, passive detectors are likely to continue to play an important role in space radiation dosimetry since there is simply no other detector which possesses the same combination of features – small size and mass, zero power and robust design being the most notable. One of the major advantages of PNTDs, such as CR-39 is its ability to accurately register the highest-LET particles ( $\sim 1000$  keV/ $\mu\text{m}$ ), a feature found only in a few other detector types.

### 3.2. Active detectors

Active detectors used aboard piloted spacecraft are mostly versions of their ground-based brethren specifically adapted for use in space. They include a number of different ion chamber-based proportional counters and solid-state charged particle telescopes. To some extent, active detectors are becoming more practical due to the reduction in size and power consumption enabled by advances in micro-electronics, increases in data storage capability and the development of longer-lived batteries. However, physics still imposes some constraints on the practicality of compact active detectors. For example, the LET of a charged particle can only be measured by a Si-detector if it stops within the volume of the detector or if two or more Si-detectors are arranged in a telescopic configuration. This imposes constraints on either the sensitive LET range or on the size and geometry of the detector. The smaller the size of a Si-detector-based telescope, the narrower is its solid

angle sensitivity and, thus, the smaller the fraction of the environment which can be sampled.

Since the early 1990s much of the useful data, including LET spectra and dose and dose equivalent measurements, characterizing the radiation environment aboard the US Space Shuttle and the Russian Mir Orbital Station have been obtained by the Johnson Space Center's Tissue Equivalent Proportional Counter (JSC-TEPC) [26]. This instrument consists of a right circular cylinder, 5.08 cm long and 5.08 cm in diameter, made of 1.9 mm thick tissue equivalent plastic and filled with low-pressure propane gas. The detector simulates a 1  $\mu\text{m}$  diameter biological cell. It is connected to a 256 channel analog to digital converter and is sensitive to ionizing particles of 0.2–1250 keV/ $\mu\text{m}$ . Resolution below 20 keV/ $\mu\text{m}$  is in 0.1 keV/ $\mu\text{m}$  steps and above 20 keV/ $\mu\text{m}$  is in 5 keV/ $\mu\text{m}$  steps. The lineal energy spectrum is recorded every minute while the absorbed dose is computed every 2 or 20 s depending on dose rate. A detector response function is then used to convert lineal energy spectrum to LET spectrum. Lineal energy transfer differs from LET in that the former accounts for the random nature of energy deposition on the microscopic scale while LET assumes a continuous linear distribution of energy deposition. In a mixed radiation field with broad range of energies and charge, the difference between the lineal energy transfer spectrum and the LET spectrum is small [26].

A plot of dose rate measured by the JSC-TEPC aboard the Mir Orbital Station as a function of orbital position superimposed on a photographic projection of the Earth's surface is shown in Fig. 11 [26]. The African continent can be seen at the center of the image, while Greenland is near the top, just left of center. The high-dose rate in the SAA is the most obvious feature. Areas of high-dose rate at the higher latitudes can also be seen. Dose rate is a minimum over equatorial regions not lying inside the SAA. Fig. 12 shows dose rate as a function of time as measured by the JSC-TEPC during the STS-63 rendezvous mission with the Mir. The small vertical oscillations correspond to the orbital passage near the equator and poles [27]. The tall peaks correspond to passage of the orbiter through the SAA. During passage through the SAA, dose rate increases from one to two

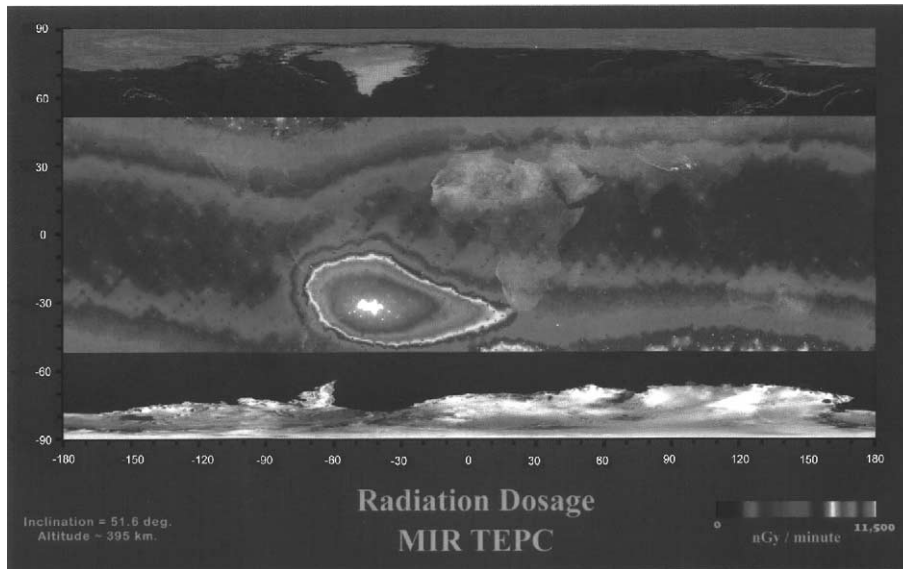


Fig. 11. Dose rate as a function of geographic latitude as measured by the JSC-TEPC aboard the Mir Orbital Station [26].

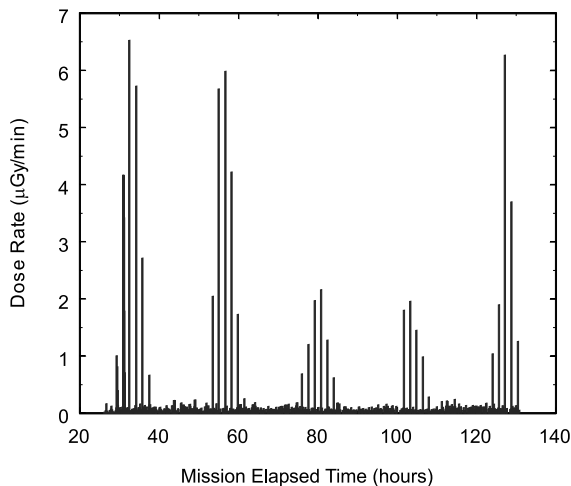


Fig. 12. Dose rate measured by the JSC-TEPC as a function of mission elapsed time during the STS-63 Mir rendezvous mission. The large peaks are from the passage of the orbiter through the SAA. The third and fourth sets of peaks are smaller than the first, second and fifth sets due to a change in the orientation of the orbiter with respect to the geomagnetic field [27].

orders of magnitude over non-SAA dose rates. Because of this large difference in dose rates, it is easy to separate the signal due to trapped particles from that produced by GCR.

Dose rate over an extended period of time has been measured aboard Mir by the R-16 operational dosimeter [28]. The R-16 consisted of two cylindrical ionization chambers, placed at right angles to each other in the Base Block of the Mir Orbital Station. Both chambers were of the IK-5 integral-pulse design and were filled with pure Ar gas at a pressure of up to  $4.5 \times 10^5$  Pa. One of the two ionization chambers, D-1, measured dose inside the Base Block while the second chamber, D-2, was behind  $3 \text{ g/cm}^2$  of tissue equivalent shielding. The instrument was capable of measuring dose rates between  $4$  and  $10^5 \text{ μGy/h}$  and had an essentially isotropic sensitivity. A similar instrument is now in operation in the main Russian module of the ISS.

Average daily dose rate as measured by the R-16 operational dosimeter over most of the 15-year history of the Mir station is shown in Fig. 13 [29]. Also shown are average crew dose rates measured using TLDs and the mean altitude of the station as a function of time. Solar cycle is shown in the form of the sunspot (Wolf) number. It is immediately clear that dose rate is anticorrelated with solar cycle. This is to be expected since the GCR flux is more fully attenuated by the increased solar wind at solar maximum. On this time-scale, little correlation can be seen between altitude and dose

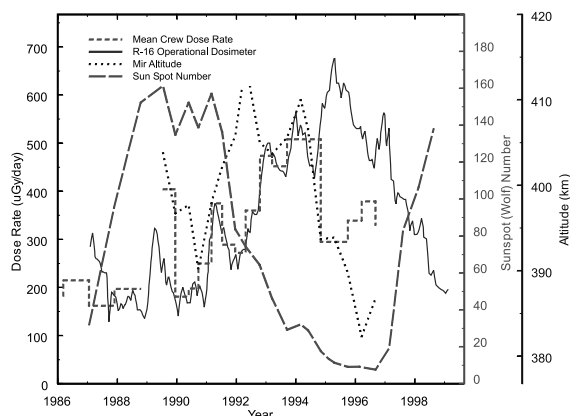


Fig. 13. Mean dose rate as measured by the R-16 operational dosimeter aboard the Mir Orbital Station over the lifetime of the Mir. Also shown is the mean altitude of the Mir, the mean crew dose rates as measured by TLDs and the sunspot number (adapted from [29]).

rate. Crew dose rates are seen to deviate substantially from the R-16 dose rate, especially during the mid-1990s. This is most likely due to the ever changing shielding environment surrounding the crew as they moved throughout the habitable volume of the station.

Three different Si-telescope-based spectrometers are in operation or are scheduled to fly aboard the ISS. The German DOSTEL (dosimeter-telescope), developed by the group of Beaujean at the University of Kiel, consists of two passivated implanted planar Si-detectors (PIPS) mounted with a 15 mm distance between them [30]. Each detector is 315  $\mu\text{m}$  thick and has a sensitive area of 692  $\text{mm}^2$ , giving DOSTEL a geometric factor of 824  $\text{mm}^2 \text{sr}$ . This telescope is sensitive to particles of LET between 0.1 and 120  $\text{keV}/\mu\text{m}$ . DOSTEL has been flown on a number of Space Shuttle missions as well as on the Euromir-97 mission and is currently operating aboard the ISS.

The Japanese real-time radiation monitoring device (RRMD-III) is a three-element telescope developed by the group of Doke at the NASDA Tskuba Space Center [31]. The RRMD-III contains three position-sensitive Si-detectors (PSD), each separated by 5 mm in a stack configuration. Each detector is 500  $\mu\text{m}$  thick and has an active area of 4  $\text{cm}^2$ . The sensitive LET range is between

0.2 and 400  $\text{keV}/\mu\text{m}$ . The top and bottom PSDs serve as triggers while energy deposition is measured by the middle detector. In addition to measuring energy deposition, the three PSDs together can provide angular information on particle trajectories with a resolution of  $3.22^\circ$ . The RRMD-III and its predecessor, RRMD-II, have been flown on several Space Shuttle missions and the RRMD-III is scheduled to be flown aboard the Japanese experiment module (JEM) on ISS.

The most sophisticated radiation monitoring instrument scheduled to fly on the ISS is the charged particle directional spectrometer (CPDS) developed by Badhwar at the NASA Johnson Space Center [32]. The CPDS contains three 1 mm thick Si-detectors used for triggering and antiscatter, four 5 mm thick Si-detectors for measuring energy deposition, a Cerenkov detector and a scintillation detector. The CPDS has been flown on several Space Shuttle flights including STS-48 where it was used to measure the energy spectra from low  $Z$  secondaries in the GCR. One CPDS will be flown within the habitable volume of ISS while two will be flown in a mutually orthogonal configuration on the truss.

There are at least two portable Si-detectors that have been specifically developed for use aboard piloted spacecraft. The Liulin mobile dosimeter unit is a portable battery-operated Si-detector developed by the group of Dachev at the Bulgarian Academy of Sciences and was first flown aboard the Mir Orbital Station in 1989 [33]. The Li-drifted Si-detector contained in Liulin has an active area of 0.5  $\text{cm}^2$  and a thickness of 300  $\mu\text{m}$ . This gives Liulin a sensitive LET range between 0.1 and 70  $\text{keV}/\mu\text{m}$ . Liulin was operating during the October 1989 SPE and obtained some of the best measurements to date of the dose rate dynamics aboard a piloted spacecraft during a major SPE. The group of Badhwar [34] at the NASA Johnson Space Center has been developing a small single detector Si diode dosimeter for use aboard the ISS. A phantom human head and torso equipped with five of these compact detectors are being flown aboard the ISS Expedition-2 mission. These detectors are calibrated to measure total dose and mean quality factor from which a value of dose equivalent can be obtained.

Although active instruments for the measurement of space radiation have become more numerous in recent years, in general they remain too large and massive for use as personal dosimeters. For example, the German DOSTEL measures  $7 \times 7 \times 10 \text{ cm}^3$  and has a mass of 0.57 kg [30]. As a consequence, active instruments tend to be fixed or rack mounted within the habitable volume of the spacecraft. The exception is the compact Si-detectors such as Liulin. These detectors possess several advantages over passive detectors in that they obtain real-time data and that data analysis tends to be less labor-intensive. However, these portable active detectors are unable to measure high-LET particles and thus will systematically underestimate the dose equivalent.

The current selection of passive and active detectors measures most of the quantities important to space radiation dosimetry. However, they remain deficient in a number of areas. Principal among these is the dosimetry of neutrons. Also the results of measurement by different instruments are often not easily intercomparable. For example, CR-39 PNTDs often measure a higher signal at  $\text{LET} \geq 100 \text{ keV}/\mu\text{m}$  than does the JSC-TEPC. This is thought to be due to differences in the atomic composition of the two detectors and the subsequent secondary charged particle spectrum they produce. While most of the detectors routinely used for space radiation dosimetry have been adequately calibrated, to date there has been no program for a systematic intercalibration and comparison of the different instruments. Such a program has just been initiated at the Japanese National Institute of Radiological Sciences, which will use the HIMAC Heavy Ion Accelerator for ground-based intercalibration studies [35].

#### 4. Review of dose measurements made in space

Much of the space radiation dosimetry data that have been acquired over the past several decades is in the form of dose or mean dose rate. This is mainly due to the fact that the quantity of dose can be readily measured by a number of different types of instruments, most notably TLDs. While dose is certainly not the best quantity by

which to characterize astronaut or spacecraft radiation exposure, it can provide much useful information concerning crew exposure as functions of orbital altitude and inclination, spacecraft shielding and orientation, and solar cycle phase. An added advantage of measuring only dose is that measurements made aboard different spacecraft, by different instruments from different research groups, and made at very different times, can be intercompared. The major drawback in measuring dose alone, especially using TLDs, is that no information concerning particle fluence and LET is recorded. Thus dose measurements made aboard spacecraft represent at best an incomplete picture of the radiation exposure received.

##### 4.1. Early Russian dose measurements

Mean dose rates measured aboard Russian spacecraft between 1960 and 1983 are summarized in Table 2 [36–38]. Absorbed dose rates measured for crews of the Russian Salyut space stations are listed in Table 3 [39]. Dose rate tends to fall between 100 and 300  $\mu\text{Gy}/\text{day}$ , reflecting the fact that early Russian piloted spacecraft flew in fairly low-altitude orbits. The major exception to this was the 1965 flight of Voskhod 2, with an apogee of 500 km, aboard which a dose of 650  $\mu\text{Gy}/\text{day}$  was measured. The measurements in Table 2 were carried out using a variety of active and passive instruments and the accuracy of these early measurements is estimated to be  $\pm 15\%$ . Measurements of crew dose rates in Table 3 were carried out using TLDs.

##### 4.2. Early US dose measurements

Absorbed dose and mean absorbed dose rate measurements made aboard early US piloted spacecraft using TLDs are presented in Table 4 [24]. The data for the Gemini, Skylab and Apollo-Soyuz Test Project (ASTP) missions reflect the strong altitude dependence of these early LEO missions. Measurements made aboard the Apollo lunar flights are the only extant data from piloted spacecraft outside the Earth's magnetosphere. The Apollo measurements reflect the

Table 2

Dose rates measured on early Russian piloted spacecraft [36–38].

Mission	Date		Orbital parameters		Mean dose rate ( $\mu\text{Gy/day}$ )
	Month	Year	Inclination ( $^{\circ}$ )	Apogee (km)	
	8	1960	65	340	125
Vostok-1	4	1961	65	330	72
Vostok-2	8	1961	65	240	84
	5	1962	65	330	160
Vostok-3	8	1962	65	370	450
Vostok-4	8	1962	65	240	135
	10	1962	65	350	300
	11	1962	65	380	300
	12	1962	65	400	350
	4	1963	65	340	180
Vostok-5	5	1963	65	370	150
Vostok-6	5	1963	65	400	300
	6	1963	65	300	120
	6	1963	65	220	155
	6	1963	65	230	155
Voskhod-1	10	1964	65	410	290
Voskhod-2	4	1965	65	500	650
	9	1965	65	360	160
	10	1965	65	340	150
	11	1965	65	350	180
	3	1966	65	310	110
	4	1966	65	330	155
	7	1966	73	350	210
	7	1966	52	360	260
	8	1966	65	360	290
	11	1966	65	340	220
	12	1966	65	320	140
Soyuz-3	11	1968	52	210	212
Soyuz-4	1	1969	52	210	200
Soyuz-5	1	1969	52	~210	240
Soyuz-6	10	1969	52	~210	140
Soyuz-7	10	1969	52	~210	130
Soyuz-8	10	1969	52	~210	140
Soyuz-9	6	1970	52	~210	130
	12	1973	52	~210	125
Salyut-3	7	1974	51.6	270	150
Salyut-4	12	1974	51.6	270	130
Salyut-5	6	1976	51.6	260	150
Salyut-6	9	1977	51.6	275	160
Salyut-6	05–06	1980	51.6	~275	100
Salyut-7	03–07	1983	51.6	340	167
Salyut-7	07–08	1983	51.6	340	148
Salyut-7	08–09	1983	51.6	340	180
Salyut-7	09–11	1983	51.6	492	160

specific trajectory taken by the spacecraft through the ERB in transit to and from the Moon. Mean dose rate for the Apollo missions ranged from 220 to 1270  $\mu\text{Gy/day}$ . The 1270  $\mu\text{Gy/day}$  dose

rate measured on Apollo 14 was the highest mission averaged dose rate until the high-altitude Hubble Space Telescope servicing missions of the Space Shuttle.



Table 3  
Crew dose rates measured using TLDs aboard the Salyut orbital stations [39]

Orbital station	Transport spacecraft	Period and duration of mission	Cosmonaut	Absorbed dose rate ( $\mu\text{Gy/day}$ )
Salyut-3	Soyuz 14	3–19 July 1974	Commander	$165 \pm 6$
		16 days	Engineer	$184 \pm 11$
Salyut-4	Soyuz 17	11 January–9 February 1975	Commander	$257 \pm 57$
		30 days	Engineer	$213 \pm 27$
Salyut-4	Soyuz 18	24 May–26 July 1975	Commander	$484 \pm 48$
		63 days	Engineer	$344 \pm 30$
Salyut-5	Soyuz 21	6 July–24 August 1976	Commander	$169 \pm 14$
		49 days	Engineer	$167 \pm 6$
Salyut-5	Soyuz 24	7–25 February 1977	Commander	$193 \pm 7$
		18 days	Engineer	$188 \pm 5$
Salyut-6	Soyuz-26	10 December 77–16 March 78	Commander	$214 \pm 10$
		96 days	Engineer	$224 \pm 8$
Salyut-6	Soyuz 29 & Soyuz 31	16 June–2 November 1978	Commander	$225 \pm 14$
		140 days	Engineer	$239 \pm 14$
Salyut-6	Soyuz 32 & Soyuz 34	25 February–19 August 1979	Commander	$210 \pm 11$
		175 days	Engineer	$210 \pm 11$
Salyut-6	Soyuz 35 & Soyuz 37	9 April–11 November 1980	Commander	$146 \pm 9$
		185 days	Engineer	$146 \pm 9$
Salyut-6	Soyuz T4	12 March–26 May 1981	Commander	$147 \pm 5$
		75 days	Engineer	$141 \pm 5$

Table 4  
Doses and mean dose rates measured using TLDs on early US piloted space missions [24]

Mission	Duration	Inclination	Apogee (km)	Perigee (km)	Absorbed dose (mGy)	Mean dose rate ( $\mu\text{Gy/day}$ )
Gemini 4	97.3 h	32.5°	296	166	0.46	110
Gemini 6	25.3 h	28.9°	311	283	0.25	230
Apollo 7	260.1 h		227.8	283.4	1.60	150
Apollo 8	147 h		Lunar orbital flight		1.60	260
Apollo 9	241 h		190	192	2.00	200
Apollo 10	192 h		Lunar orbital flight		4.80	600
Apollo 11	194 h		Lunar flight		1.80	220
Apollo 12	244.5 h		Lunar flight		5.80	570
Apollo 13	142.9 h		Lunar orbital flight		2.40	400
Apollo 14	216 h		Lunar flight		11.40	1270
Apollo 15	295 h		Lunar flight		3.00	240
Apollo 16	265.8 h		Lunar flight		5.10	460
Apollo 17	301.8 h		Lunar flight		5.50	440
Skylab 2	28 days	50°		Mean alt = 435	15.96	570
Skylab 3	59 days	50°		Mean alt = 435	38.35	650
Skylab 4	90 days	50°		Mean alt = 435	77.40	860
ASTP	216 h	50°		Mean alt = 220	1.06	120

#### 4.3. Dose measured aboard the Space Shuttle using TLDs

Each Space Shuttle crew member wears a crew passive dosimeter (CPD) containing an array of TLDs and, until recently, several layers of CR-39 PNTD. In addition, six area passive dosimeters (APDs) are flown at fixed locations within the Shuttle orbiter. These locations are referred to as DLOC1–DLOC6 and are illustrated in Fig. 14 [24]. Mean absorbed dose rate measurements made at the six APD locations as well as an estimate of the mean GCR dose rate are plotted in Fig. 15 for all Space Shuttle missions through July 1998 [40]. Most of the dose measured on the 28.5° inclination missions was from trapped protons in the SAA, while GCR makes a larger contribution to dose on more highly inclined missions. On average, dose rate has varied between 50 and 300  $\mu\text{Gy/day}$ . The exceptions are the few high-altitude (>480 km), 28.5° inclination missions, aboard which dose rates in excess of

1000  $\mu\text{Gy/day}$  were measured. These include the Hubble Space Telescope servicing missions and represent the highest mean dose rates measured aboard any piloted spacecraft to date. The reason for the high-dose rates measured on these missions is the exponential dependence of dose rate from trapped protons on altitude within the SAA.

The consistent measurement of dose by TLDs at fixed locations within the Space Shuttle orbiter has permitted the correlation of various physical parameters with dose rate. Most of the variations amongst the dose rates at the six locations are due to differences in shielding. The lowest mean dose rate tends to be measured at DLOC1 which has the greatest shielding, while the highest mean dose rate tends to be measured at DLOC2 with the least shielding. However, this is not always the case. In missions where the orbiter flew in a fixed orientation, effects besides shielding can be seen. This includes the east/west trapped proton anisotropy (*infra vide*).

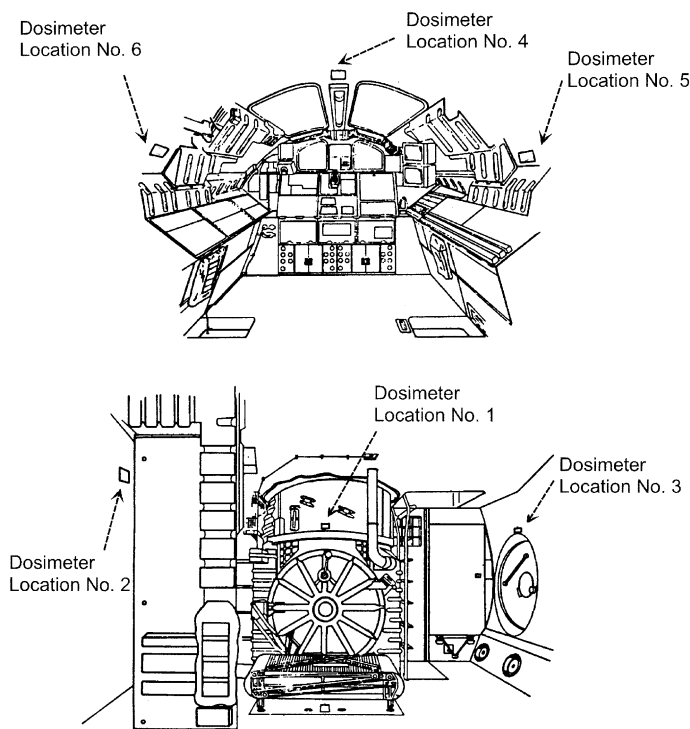


Fig. 14. The six permanent locations (DLOC) of area passive dosimeters aboard the middeck of the Space Shuttle [24].

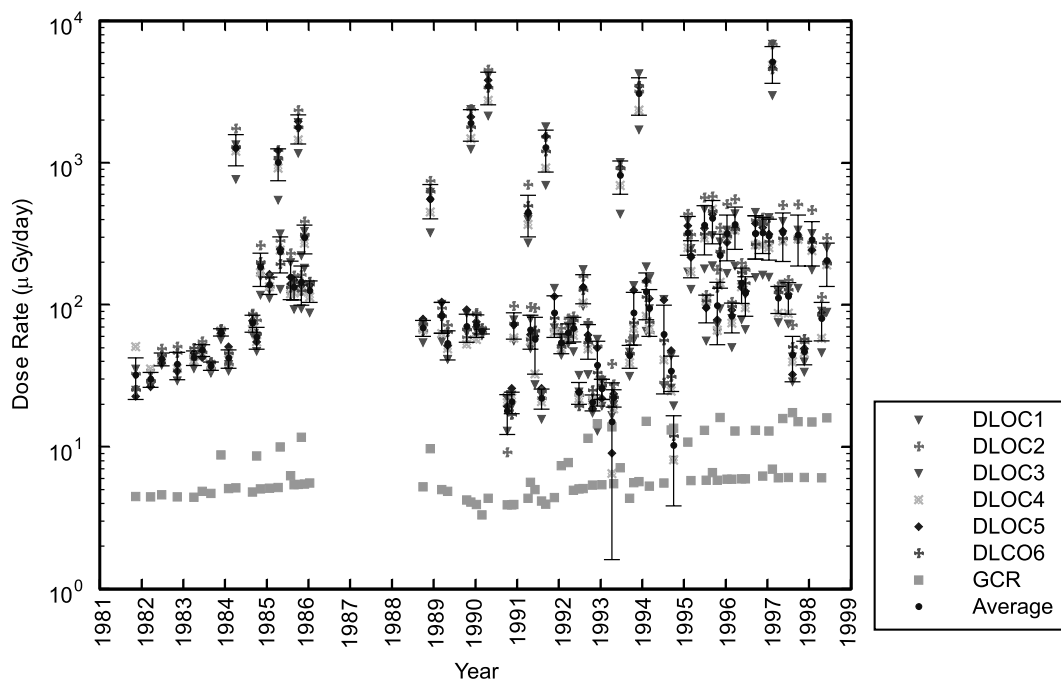


Fig. 15. Mean dose rates measured by TLDs at the six DLOC locations aboard the Space Shuttle over the history of the STS program [40].

#### 4.4. Dose measurements aboard the Mir Orbital Station

Crew dosimetry aboard the Mir was carried out using TLDs. Averaged crew doses and dose rates are given in Table 5 for each Mir mission beginning in 1986 [41]. The largest dose rate, 508  $\mu\text{Gy/day}$ , was measured on the Mir-15 mission in 1994. Note also the dose rate of 404  $\mu\text{Gy/day}$  measured on Mir-5 and coinciding with the 1989 SPEs. In general there was a factor of between 1.2 and 1.4 difference in dose between the two individual crew members, due largely to differences in shielding surrounding each of the two crew members over the duration of the mission.

Benton and Benton [42] have collected and tabulated mean dose rate measurements made using TLDs at various locations inside the Mir Base Block for which average shielding has been calculated. Tables 6 and 7 contain a representative sample of these data, while Fig. 16 shows the locations and shielding where these dose rate measurements were made. The measurements were

carried out over periods ranging from days to months, and at very different times, sometimes separated by years. Differences in dose rates measured at a specific location reflect changes in a number of different variables including the solar cycle phase, differences in the spacecraft altitude and attitude, and local shielding conditions as equipment was installed and removed. Dose rate at Location No. 1 inside the Commander's cabin varied from 410  $\mu\text{Gy/day}$  in mid- to late-1995 to 514  $\mu\text{Gy/day}$  in mid-1996 [43–45]. Similarly, dose rates at Location No. 2 in the Flight Engineer's cabin varied from 201  $\mu\text{Gy/day}$  to 454  $\mu\text{Gy/day}$ , a difference of greater than a factor of 2, over a period lasting from May 1991 to May 1997 [43–46].

Change in altitude is probably the single largest factor contributing to the differences in dose rate measured at the same location inside the Mir Base Block over an extended period of time. However, changes in shielding also play a major part. The shielding environment inside the station was constantly changing. Over the course of its history, the Mir was expanded from the single Base Block to a

Table 5

Mir crew doses and mean dose rates measured using TLDs [41]

Mission	Launch date	Duration (days)	Altitude (km)	Dose (cGy)	Dose rate ( $\mu\text{Gy/day}$ )
Mir-01	3/13/86	123	—	2.24	182
Mir-02	2/6/87	217	—	4.67	215
Mir-03	12/26/87	366	—	5.95	162
Mir-04	11/26/88	152	—	2.99	197
Mir-05	9/6/89	225	403.8	6.75	404
Mir-06	2/11/90	179	396.7	3.24	181
Mir-07	8/1/90	131	397.7	2.6	198
Mir-08	12/2/90	176	390.2	4.4	250
Mir-09	5/18/90	145	398	5.44	375
Mir-10	10/2/91	175	402.2	5.05	289
Mir-11	3/17/92	146	405.8	3.97	272
Mir-12	7/27/92	190	414.5	6.85	360
Mir-13	1/26/93	180	405	8.54	474
Mir-14	7/1/93	197	403.7	8.91	452
Mir-15	1/8/94	183	405.6	9.29	508
Mir-16	7/1/94	126	410	—	—
Mir-17	10/4/94	169	406.6	—	—
Mir-18	3/14/95	115	393.7	3.39	295
Mir-20	9/3/95	179	393.9	—	—
Mir-21	2/21/96	195	389.8	6.62	339
Mir-22	8/17/96	198	382.3	7.5	379
Mir-23	2/10/97	187	386.8	6.15	329

Table 6

Location no. 1: commander's cabin, outer wall, mean shielding =  $18.6 \text{ g/cm}^2$  [42–45]

Experiment/institution	Dates	Duration (days)	Dose (mGy)	Dose rate ( $\mu\text{Gy/day}$ )
Mir-19/ISDA TLD-600	6/27/95–11/20/95	145	$61.9 \pm 1.4$	$427 \pm 10$
Mir-19/ISDA TLD-700	6/27/95–11/20/95	145	$59.5 \pm 1.1$	$410 \pm 8$
NASA-2/JSC	3/22/96–9/26/96	188.2	$96.8 \pm 0.9$	$514 \pm 5$
NASA-3/JSC	9/16/96–1/22/97	127.2	$53.9 \pm 0.7$	$421 \pm 4$

complex consisting of six separate modules. Much of the scientific research carried out aboard Mir was centered in the Base Block. This means that much equipment was constantly being moved into and out of the habitable volume near the locations where doses were measured and for which shielding was calculated.

## 5. Survey of the LEO radiation environment

### 5.1. Dependence on orbital inclination

The relative contributions from GCR and trapped protons to the overall radiation exposure

of a spacecraft in LEO are dependent in part on the inclination of the orbit with respect to the Earth's equator. For highly inclined orbits (orbits which take the spacecraft near the magnetic poles) GCR tends to dominate since GCR is funneled along the lines of the geomagnetic field and since the average amount of a time a spacecraft spends traversing the SAA as a fraction of total orbital period is a minimum. Conversely, in orbits of lower inclination (orbits that remain near the Earth's equator) trapped protons from the SAA are the single largest radiation source. Not only does the spacecraft spend, on average, a larger fraction of each orbit passing through the SAA, but the geomagnetic cutoff prohibits all but the

Table 7

Location no. 2: engineer's cabin, outer wall, mean estimated shielding = 22 g/cm<sup>2</sup> and ADLET Position 1: forward wall of engineer's cabin, mean shielding = 25.9 g/cm<sup>2</sup> [42–45]

Experiment/institution	Dates	Duration (days)	Dose (mGy)	Dose rate (μGy/day)
DosiMir 1/ISDA	5/91–10/91	145	34.8±1.2	240 ± 8
DosiMir 2/ISDA	10/91	8	1.6±0.2	201 ± 3
DosiMir 2/IMBP	10/91	8	1.7±0.1	218 ± 10
Mir 92/DLR	1992			205 ± 6
				208 ± 5
				229 ± 13
				294 ± 13
ADLET-1/ISDA	1/94–7/94	182	55.0±1.8	302 ± 10
ADLET-1/IMBP	1/94–7/94	182	59.2±4.9	325 ± 27
EuroMir 94/DLR	1994			380 ± 7
				322 ± 4
ADLET-2/ISDA	1/94–11/94	300	90.3±3.0	301 ± 10
ADLET-2/IMBP	1/94–11/94	300	83.4±5.1	278 ± 17
ADLET-3/ISDA	1/94–3/95	437	125.9±4.4	288 ± 10
ADLET-3/IMBP	1/94–3/95	437	130.7±9.2	299 ± 21
EuroMir 95/DLR	1995			483 ± 8
				371 ± 3
NASA-2/JSC	3/22/96–9/26/96	188.2	73.5±0.8	391 ± 4
Mir-19/ISDA TLD-600	6/27/95–11/20/95	145	65.6±2.9	452 ± 20
Mir-19/ISDA TLD-700	6/27/95–11/20/95	145	6408±4.7	447 ± 32
Pille 95/KFKI	1995			247 ± 10
Mir 97/DLR	1997			461 ± 4
				370 ± 3
NASA-3/JSC	9/16/96–1/22/97	127.2	43.6±0.7	341 ± 4
NASA-4/KFKI	1/12/97–5/22/97	130.1	57.1±5.3	439 ± 41
			59.1±5.6	454 ± 43

most energetic GCR from penetrating to these low latitudes.

The dependence of a spacecraft's radiation exposure on orbital inclination can be illustrated by looking at the LET spectra measured by the JSC-TEPC and USF CR-39 PNTDs on a number of different Space Shuttle missions. Fig. 17 shows the mean integral LET flux spectra measured on STS-57, a 28.5° inclination, 462 km altitude mission [47]. This is an example of the lowest-orbital inclination in which the Space Shuttle can be launched, dictated by the fact that the Kennedy Space Center lies at 28.5° north latitude. There is close agreement between the USF LET spectrum and the total spectrum measured by the JSC-TEPC. The JSC-TEPC spectrum from trapped protons is nearly identical with the total, while the GCR spectrum lies nearly an order of magnitude lower. The trapped proton spectrum is that measured when the Shuttle was passing through the SAA,

while the GCR spectrum is that measured at all other times. Because the Shuttle did not reach high latitudes, GCR contribution was reduced by the geomagnetic cutoff. In addition, lower-inclination orbits take the Shuttle through a wider portion of the SAA and thus increase the average amount of time per orbit spent in the SAA.

The integral LET flux spectra shown in Fig. 18 were measured on STS-60 in a 57° inclination, 353 km altitude orbit [48]. An orbital inclination of 57° is about the most steeply inclined orbit into which the Space Shuttle can be launched from the Kennedy Space Center, with a launch trajectory that takes the Shuttle just east of the eastern seaboard of the US. Again, there is good agreement between the LET spectra measured by the USF CR-39 PNTDs and the JSC-TEPC. At LETs above 10 keV/μm, GCR is seen to dominate over trapped protons. The two curves tend to diverge at the highest LETs (>400 keV/μm), but this may in part

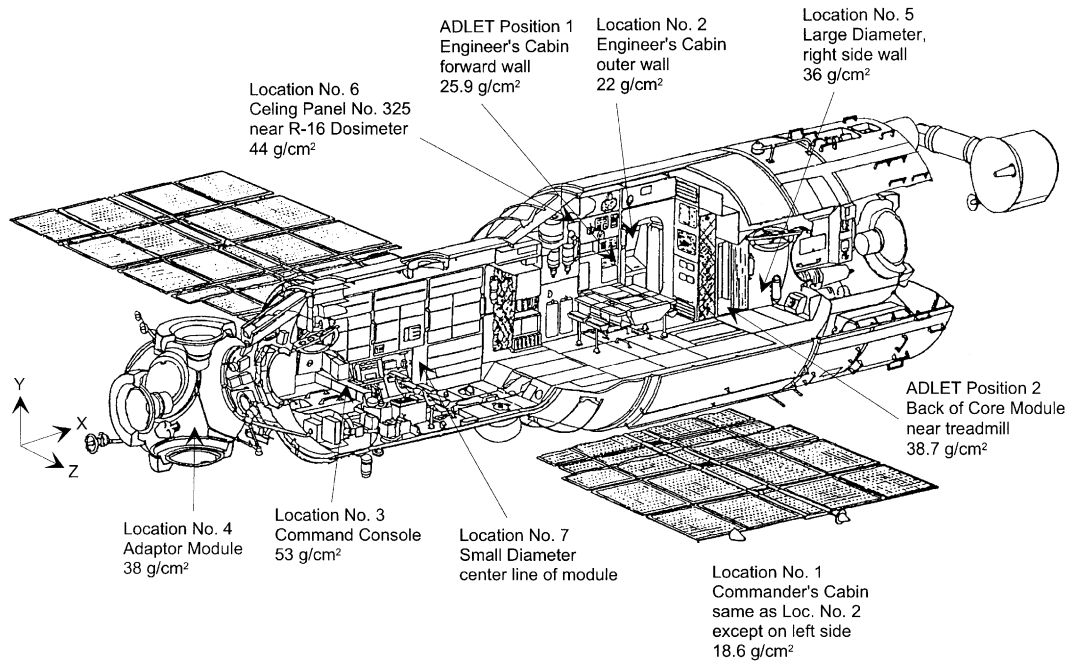


Fig. 16. Locations and shielding of passive detectors within the Base Block of the Mir Orbital Station [42].

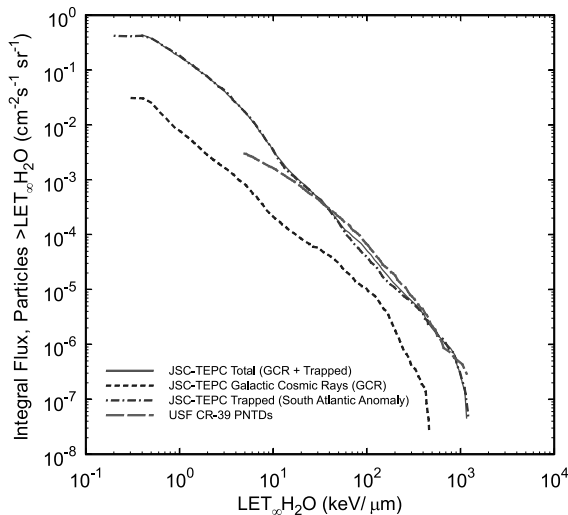


Fig. 17. Integral LET flux spectra measured by the JSC-TEPC and USF CR-39 PNTDs on the 28.5°, 462 km altitude STS-57 mission in June 1993 [47].

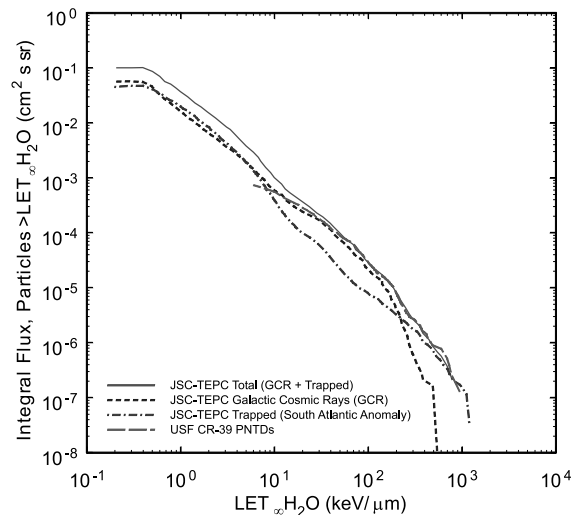


Fig. 18. Integral LET flux spectra measured by the JSC-TEPC and USF CR-39 PNTDs on the 57°, 353 km altitude STS-60 mission in February 1994 [48].

be due to the small number of high-LET particles. For LET less than  $\sim 10$  keV/ $\mu$ m, the contributions of GCR and trapped protons are about the same.

Fig. 19 shows the integral LET flux spectra measured on STS-63, a Mir rendezvous mission with an orbital inclination of 51.56° and an altitude of

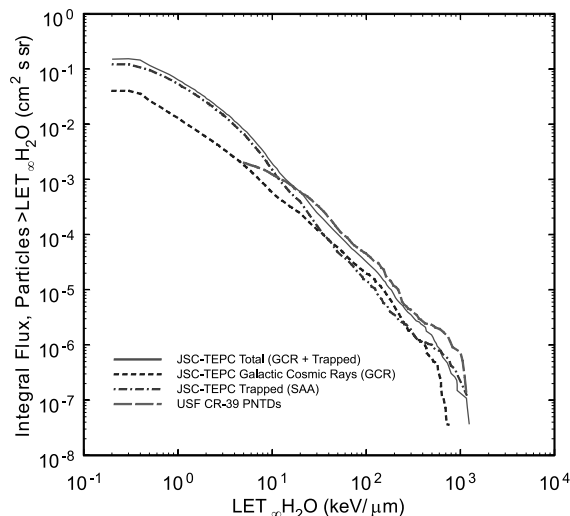


Fig. 19. Integral LET flux spectra measured by the JSC-TEPC and USF CR-39 PNTDs on the 51.56°, 400 km altitude STS-63 Mir rendezvous mission in February 1995 [27].

~400 km [27]. This spectrum is similar to that measured on STS-60. In the 51.56° inclination, ~400 km altitude orbit of Mir and ISS, the contribution from GCR and trapped protons to total dose is roughly equal.

### 5.2. Altitude dependence

The radiation exposure of a spacecraft in LEO is highly dependent upon the altitude, especially the altitude at which it traverses the SAA. In the SAA, flux increases exponentially with altitude as illustrated by Fig. 20. Fig. 20 shows the integral LET flux spectra measured by the JSC-TEPC during the STS-63 mission at four different altitudes while passing through the SAA [27]. This altitude dependence holds over the entire range of spectra measured. There is little difference between the spectra measured at 391 and 379 km. However the spectra measured at 347 and 338 km fall substantially lower. Differences in the orientation of the orbiter as it passed through the SAA and the corresponding changes in the direction of shielding surrounding the TEPC relative to the SAA are responsible for the spectrum measured at 338 km lying above that measured at 347 km.

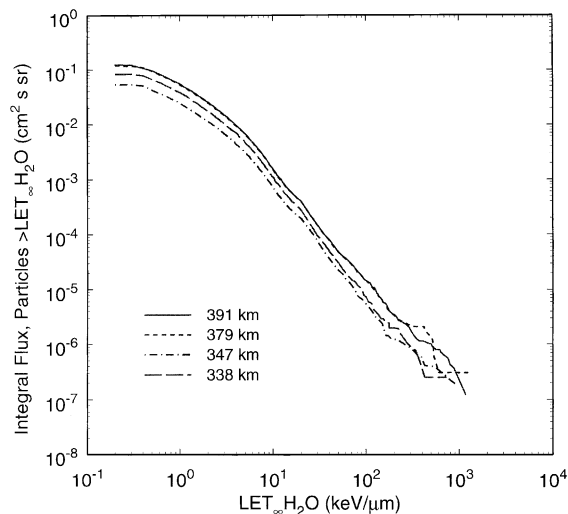


Fig. 20. Integral LET flux spectra measured by the JSC-TEPC at four altitudes inside the SAA during the STS-63 Mir rendezvous mission in February 1995 [27].

Altitude is one of the most sensitive parameters in determining dose rate and it has been on high altitude, 28.5° inclination Space Shuttle missions where the highest mean dose rates aboard piloted spacecraft have been measured. Fig. 21 shows mean dose rate as functions of altitude and atmospheric density, respectively, for Shuttle missions of three different orbital inclinations [40]. While dose rate can be seen to increase with altitude, this trend is not so apparent for dose rate as a function of decreasing atmospheric density, especially for the 28.5° inclination missions. Atmospheric density is affected by the solar wind and tends to increase at a given altitude during the maximum phase of the solar cycle.

### 5.3. East/west trapped proton anisotropy

The proton flux encountered by a spacecraft as it traverses the SAA is anisotropic. Protons traveling toward the east are following geomagnetic field lines (or guiding centers) above the spacecraft's orbit, while protons traveling toward the west are following geomagnetic field lines that lie below the spacecraft's orbit. The radius of the cyclotron motion of energetic protons in the SAA is of the same order as the height of the atmo-

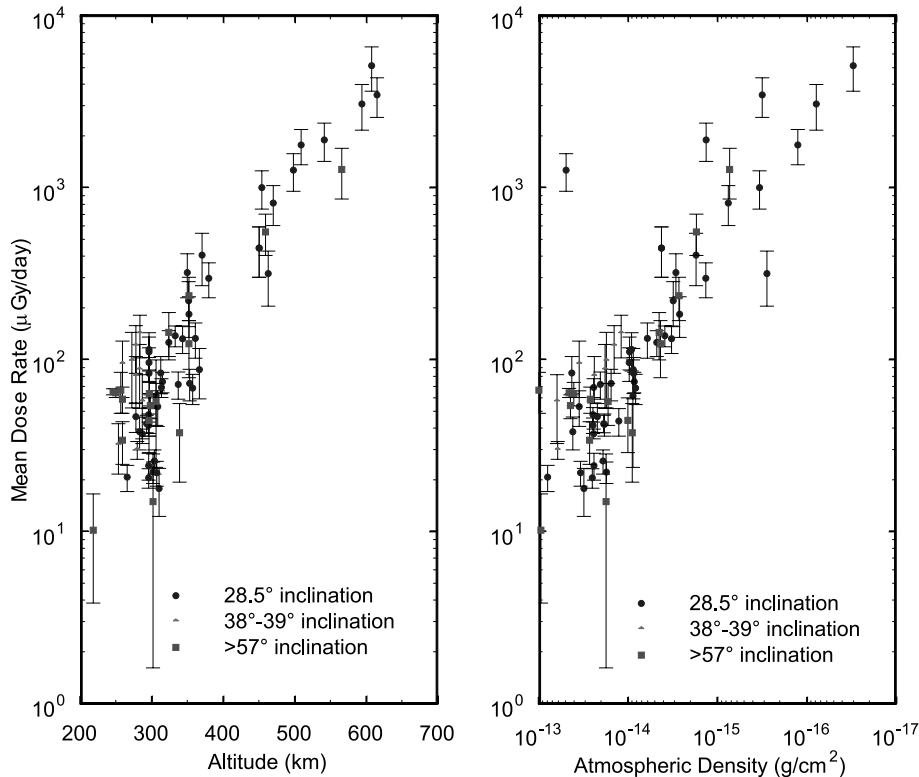


Fig. 21. Mean dose rate as functions of altitude (left) and atmospheric density (right) measured aboard the Space Shuttle in three different inclination orbits [40].

sphere (atmospheric density scale height). Particles traveling toward the west traverse a significantly denser portion of the atmosphere than do particles traveling toward the east and are thereby more likely to undergo interactions with the atmosphere and be attenuated. This phenomenon is referred to as the east/west trapped proton anisotropy. For spacecraft such as the Space Shuttle that typically have no fixed orientation relative to the geomagnetic field when they pass through the SAA, the effects of the trapped proton anisotropy tend to be averaged out over the duration of the mission. For spacecraft such as ISS that are in a fixed orientation relative to the geomagnetic field, the east/west trapped proton anisotropy can lead to differences of up to a factor of 3 in dose rate between the west and east sides of the spacecraft.

The east/west trapped proton anisotropy was evident in TLD dose measurements made aboard

the NASA Long-Duration Exposure Facility (LDEF). LDEF was a gravity-gradient stabilized satellite that was placed into 28.5° inclination orbit in 1984 and retrieved nearly six years later in 1990. Fig. 22 shows dose as a function of shielding depth for two detector sets located on the east side of the LDEF (M0004 Experiment) and one detector set on the west side of the satellite (P0006 Experiment) [49]. Under similar shielding depths, dose on the west side (from particles traveling toward the east) is about a factor of 3 greater than that measured on the east side (from particles traveling toward the west).

A similar result was observed by Badhwar aboard the STS-63 Space Shuttle mission in a 51.56° inclination, ~400 km altitude, Mir rendezvous orbit [27]. Two active autonomous dosimeters (AADs), each containing a Si detector, were mounted inside the middeck of the Shuttle, one on



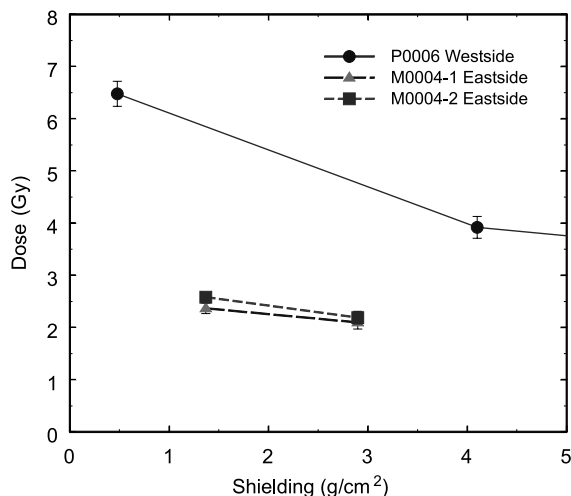


Fig. 22. Dose measured by TLDs on the west and east sides of the LDEF, illustrating the east/west trapped proton anisotropy. West and east doses differ by a factor of  $\sim 3$  [49].

the left or port wall of the orbiter and the other on the right or starboard wall of the orbiter. These detectors were sensitive in an energy interval be-

tween 0.3 and 10 MeV. Fig. 23 shows dose rate as a function of mission elapsed time for the two ADDs while the Shuttle was traversing the SAA. The maximum ratio between port and starboard dose rates was 2.7. More recently Badhwar has measured an east/west dose rate ratio of  $\sim 2.7$  using the JSC-TEPC on the  $28.5^\circ$  STS-94 Space Shuttle mission [50].

#### 5.4. Dependence on spacecraft shielding

Spacecraft shielding is one of the most important factors in determining the characteristics of the space radiation field inside a spacecraft. The complex role played by a spacecraft's shielding can be illustrated by results from detectors exposed by USF aboard the Mir Orbital Station. A series of integrating measurements of environmental radiation using passive dosimeters located throughout the interior of the Mir was carried out as part of the NASA–Mir Phase 1B Science Program in 1996–1997. Area passive dosimeters were mounted at six locations inside the Mir during three of the

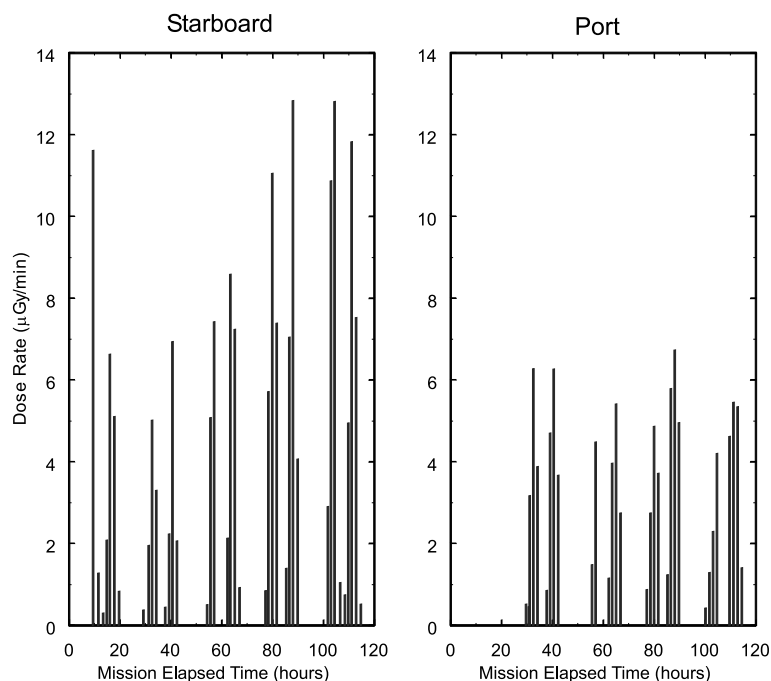


Fig. 23. Dose rate measured on the port and starboard sides of the Space Shuttle middeck during the STS-63 mission. Starboard and port dose rates differ by a factor of 2.7 due to the east/west trapped proton anisotropy [27].

seven NASA/Mir missions. The APDs were switched out with fresh dosimeters during the Shuttle docking missions and exchange of US astronauts. Each APD contained CR-39 PNTDs oriented in three mutually orthogonal directions and two arrays of TLD-700. Two APD locations are of special interest. APD-2 was located in the large diameter section of the Base Block on a ceiling panel directly beneath the R-16 operational dosimeter. It was therefore behind a fairly large amount of equipment and the shielding is estimated to have been in excess of  $40 \text{ g/cm}^2$ . APD-3 was located near Window No. 3, beneath the command console in the small diameter of the Base Block. Being located quite close to the skin of the spacecraft, shielding is estimated to have been less than  $20 \text{ g/cm}^2$ .

The integral LET flux spectra measured aboard the Mir during the NASA-4/Mir-23 mission are shown in Fig. 24. This mission lasted 134 days, beginning on 12 January 1997 and ending on 22 May 1997 [42]. For LET less than  $\sim 100 \text{ keV}/\mu\text{m}$ , there is fairly close agreement between the two spectra. Above  $100 \text{ keV}/\mu\text{m}$ , the curve from the more heavily shielded APD-2 lies significantly above that of the less shielded APD-3. In other words, high-LET flux at the more heavily shielded

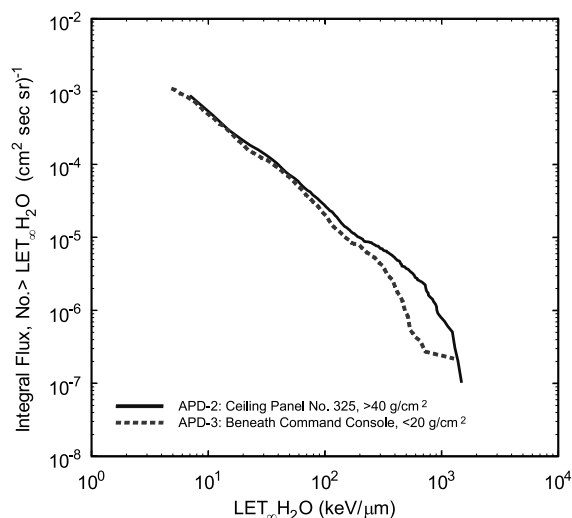


Fig. 24. Integral LET flux spectra measured by USF using CR-39 PNTDs at two locations inside the Mir Orbital Station during the NASA-4/Mir-23 mission in 1997 [42].

location was greater than at the less shielded location. This difference is amplified in the integral LET dose rate spectra shown in Fig. 25. Here the APD-2 curve lies above the APD-3 curve over the entire measured range. Similarly, in the integral LET dose-equivalent rate spectra shown in Fig. 26,

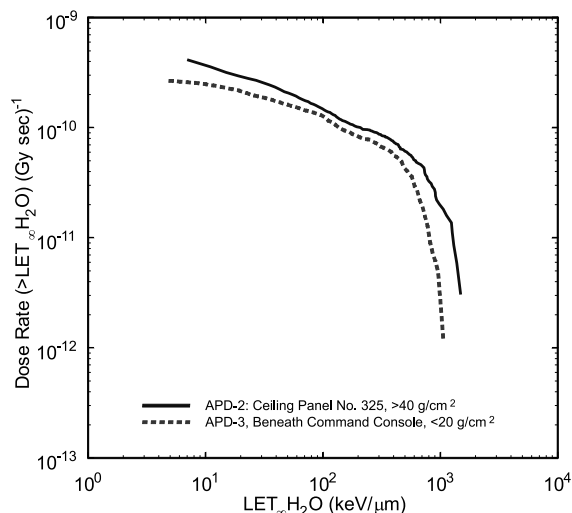


Fig. 25. Integral LET dose rate spectra measured by USF using CR-39 PNTDs at two locations inside the Mir Orbital Station during the NASA-4/Mir-23 mission in 1997 [42].

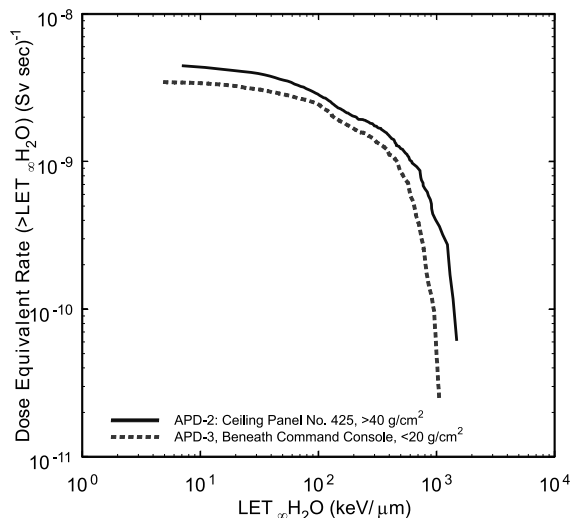


Fig. 26. Integral LET dose-equivalent rate spectra measured by USF using CR-39 PNTDs at two locations inside the Mir Orbital Station during the NASA-4/Mir-23 mission in 1997 [42].

the slope of the curves is quite steep at high-LETs and level off rapidly below 100 keV/μm. The APD-2 curve lies completely above that of APD-3 since the LET dependence of the quality factor enhances the contribution of high-LET particles to the integral spectrum.

Mean dose rates and dose equivalent rates, and mean quality factors were measured in the five Mir APDs during the NASA-4/Mir-23 mission using combined TLD and CR-39 PNTD and the results are shown in Table 8. Also shown are the relative contributions to dose and dose equivalent from particles of LET  $\geq 5$  keV/μm – that is from the CR-39 PNTD measurements. Mean dose rate measured in APD-3 under less than 20 g/cm<sup>2</sup> was 375 μGy/day, while a mean dose rate of 307 μGy/day was measured in APD-2, behind an excess of 40 g/cm<sup>2</sup>. However, the mean dose-equivalent rates measured in these two locations are, within measurement uncertainty, the same: ~650 μSv/day. The mean quality factor for APD-2 is 2.1 as compared to 1.7 for APD-3. Particles of LET  $\geq 5$  keV/μm contributed 6% of the dose under low shielding, and 12% of the total dose in the more heavily shielded detector. Contribution to dose equivalent from particles of LET  $\geq 5$  keV/μm was 30% in APD-3, but nearly 60% in APD-2.

Lower shielding yields higher dose rates while greater shielding yields a higher mean quality factor. In other words, increased shielding serves to “harden” the spectrum. This phenomenon is largely the result of proton-induced target fragmentation and the high-LET ( $\geq 100$  keV/μm) portion of the spectrum in large part consists of short-range secondary particles produced in nuclear interactions between the trapped protons in the SAA and the constituent nuclei of the spacecraft. Fig. 27 shows the integral LET flux spectrum measured in APD-2 during the NASA-2/Mir-21 mission. Particles that formed tracks on only a single surface of the detector have been separated from those that formed tracks on both the top and bottom surfaces of the detector. The single surface events are largely from target fragment secondaries while the two surface events include the primary GCR component. Below ~400 keV/μm, the single surface target fragments, not the two surface HZE particles, are the dominant component.

Table 8

Measured dose rates and dose-equivalent rates on the NASA-4/Mir-23 mission (1/12/97–5/24/97, 132.1 days) using TLDs and CR-39 PNTDs, and contributions to total dose rates and dose-equivalent rates from particles, including target fragments, of LET  $\geq 5$  keV/μm [42]

Detector no.	Location	Dose rate (μGy/day)	Dose rate $\geq 5$ keV/μm (μGy/day)	$\geq 5$ keV/μm contribution to dose (%)	Dose equivalent rate (μSv/day)	Dose equivalent rate $\geq 5$ keV/μm (μSv/day)	$\geq 5$ keV/μm contribution to dose equivalent (%)	Mean quality factor
APD-1	Core, door to engineer's cabin	341 ± 8	32.7 ± 1.1	9.6	678 ± 21	368 ± 18	54	2.0 ± 0.1
APD-2	Core, ceiling panel #325	307 ± 7	35.9 ± 1.3	11.7	656 ± 23	385 ± 21	58	2.1 ± 0.1
APD-3	Core, beneath command console	375 ± 9	23.0 ± 0.6	6.1	653 ± 13	247 ± 16	38	1.7 ± 0.1
APD-4	Adaptor, near window #14	321 ± 7	36.9 ± 1.0	11.4	659 ± 21	375 ± 22	57	2.1 ± 0.1
APD-6 <sup>a</sup>	Kvant 2, ceiling panel #303	304 ± 7	32.3 ± 1.1	10.6	624 ± 19	323 ± 19	52	2.1 ± 0.1

<sup>a</sup> APD-6 was exposed for both the NASA-4 and NASA-5 missions for a total of 267.5 days.

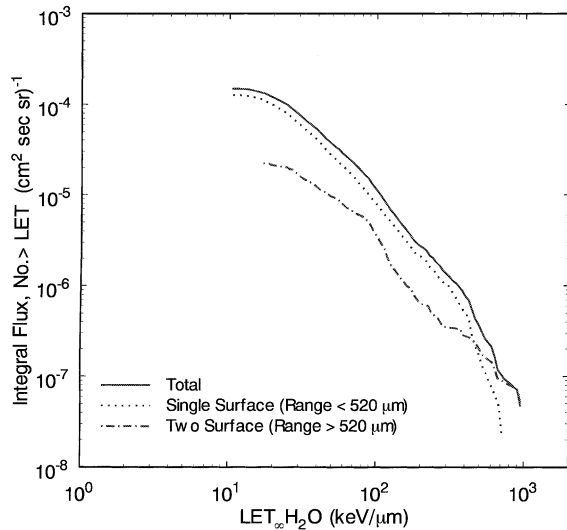


Fig. 27. Integral LET flux spectra measured in the APD-2 location aboard Mir by USF using CR-39 PNTDs. The single surface events are those that formed tracks on only the top surface of the CR-39 layer, while the two surface events are those that formed tracks on both surfaces.

### 5.5. Neutron dosimetry in LEO

The primary difficulty in designing a neutron dosimeter for use aboard piloted spacecraft is the discrimination between neutrons and the comparatively high fluxes of both primary charged particles in the form of trapped protons and GCR and secondary charged particles produced in target and projectile fragmentation. Because neutrons are uncharged, they are detected only via the secondary charged particles produced in interactions with the material through which they are passing. These “secondaries of secondaries” constitute only a fraction of the total charged particle flux.

The Benton group at USF has made neutron dose-equivalent measurements, shown in Table 9, using passive detectors by USF aboard a number of different spacecraft [51]. Neutrons of energy <1 MeV were measured using thermal/resonance neutron detectors (TRNDs) that exploit the  $^6\text{Li}(n,T)\alpha$  reaction. The TRNDs consist of a pair of detectors, one covered by a Gd foil to permit discrimination of the thermal and resonance components. Neutrons of energy >1 MeV were

Table 9  
Measurements of neutron dose equivalent made aboard various spacecraft by the University of San Francisco [51]

Mission	Launch date	Altitude (km)	Inclination (°)	Neutron energy			Mean total neutron $H^*(10)$ rate ( $\mu\text{Sv/day}$ )	Mean absorbed dose rate in TLDs ( $\mu\text{Gy/day}$ )	Neutron contribution to total $H^*(10)$ (%)
				<0.2 eV	0.2 eV–1 MeV	>1 MeV			
STS-3	3/22/82	280	40.3	0.04 ± 0.01	3.11 ± 1.51	4.5	7.7	65 ± 2	10.6
STS-4	6/27/82	297	28.5	0.06 ± 0.02	2.86 ± 1.42	8.8	11.7	63 ± 2	15.7
STS-5	11/11/81	297	28.5	0.06 ± 0.02	1.72 ± 0.86	9.7	11.5	56 ± 5	17.1
STS-6	4/4/83	284	28.5	0.06 ± 0.02	4.66 ± 2.33	5.73	10.5	55 ± 2	16.0
STS-41A	11/28/83	241	57						
SL-1 Module				0.01 ± 0.01	3.03 ± 1.49	19.3	22.3	100 ± 10	18.3
SL-1 Pallet				0.01 ± 0.01	8.87 ± 4.41	20.68	30.0	184 ± 7	13.8
STS-51F	7/29/85	322/304	49.5	0.05 ± 0.02	14.66 ± 7.33	19.06	33.8	313 ± 15	9.7
Cosmos-936	8/3/77	419/224	62.8	0.06 ± 0.02	3.90 ± 1.95	32.0	36.0	237 ± 5	13.2
Cosmos-1129	9/25/79	394/226	62.8	0.09 ± 0.03	4.87 ± 2.41	31.9	36.8	187 ± 28	16.5
Cosmos-2044	9/15/89	294/216	82.3	0.18 ± 0.06	3.03 ± 1.49	15.5	18.7	83 ± 6	18.4
LDEF	4/6/84	478	28.5						
A0015 Earthside				0.02 ± 0.01	1.40 ± 0.70	172.2	173.6	2370 ± 120	6.8
A0015 westside				0.02 ± 0.01	0.96 ± 0.48	70.6	71.6	1180 ± 60	5.7
P0006 westside				0.06 ± 0.02	4.06 ± 1.96	97.3	101.4	946 ± 47	9.7

measured using fission foil neutron detectors (FFNDs) that use the  $X(n, ff)$  reaction, where  $X$  is the nucleus of a heavy element such as Bi or Th and  $ff$  is the fission fragment produced in the reaction with a high-energy neutron.

A comparison of low-energy ( $<1$  MeV) with high-energy ( $>1$  MeV) neutron measurements indicates that the larger fraction of the neutron dose equivalent in spaceflight is consistently in the high-energy region. In addition, thermal neutrons make only a negligible contribution to dose equivalent. On the LDEF mission more than 98% of the average measured neutron ambient dose equivalent was in the high-energy region. For the Biocosmos missions this value was 87%; for four Shuttle flights (middeck locker) the high-energy neutron contribution dominated by 73%; and on Spacelab it was 71%. In general, the low-energy component increases as shielding thickness increases.

Also shown in Table 9 is a comparison between mean neutron dose-equivalent rates and mean absorbed dose rates as measured by TLDs. The absorbed dose rates measured by TLDs have not been corrected for the contribution of high-LET particles, making them systematically low by a few percent. For purpose of this comparison, the assumption is made that high-LET particles make only a negligible contribution to the charged particle dose equivalent and that a quality factor of 1 can be assigned to the TLD dose. While this assumption is not strictly correct, it is useful in giving an approximation of the relative contribution of neutrons to total dose equivalent. Neutron contributions to total dose equivalent varied from 5.7% to 18.4%, depending on shielding and mission orbit – somewhat lower than the 15–60% contribution predicted by model calculations.

A technique to measure the neutron energy spectrum between 1 and  $\sim 20$  MeV using photographic nuclear emulsions has been developed and used by Dudkin et al. [52] of the Research Center for Spacecraft Radiation Safety in Moscow. This technique exploits the elastic interactions between neutrons and the free hydrogen nuclei in the emulsion. Because of the difficulty inherent in measuring neutrons in space, results from this method present some of the few neutron spectra ever measured on the interior of a piloted space-

craft. Fig. 28 shows neutron spectra measured aboard four  $28.5^\circ$  inclination Space Shuttle missions [17]. Three of the four missions were at a similar altitude of  $\sim 300$  km, while STS-57 was at a much higher altitude of 470 km. All four missions occurred within a 3-year period approaching solar minimum. Below 5 MeV all four spectra show a rapid decrease in differential neutron flux with increasing neutron energy. The flux above 5 MeV was found to be significantly higher on the high-altitude STS-57 mission than on the other three missions, indicating that the major source of these neutrons is from trapped protons encountered in the SAA. The poor agreement amongst the remaining curves above 5 MeV is probably due to differences in shielding surrounding the emulsion packages during the three missions.

Dose rates and ambient dose-equivalent rates measured in emulsion during the four Shuttle missions are shown in Table 10. Also shown are the mean crew dose and dose-equivalent rates, measured using TLD-100, corrected for high-LET particle contribution using results from the JSC-TEPC, and the relative contributions from neutrons to total dose rate and dose-equivalent rate. Neutron contribution to dose rate varied from 3.65% to 14.6%. However, the neutron contribu-

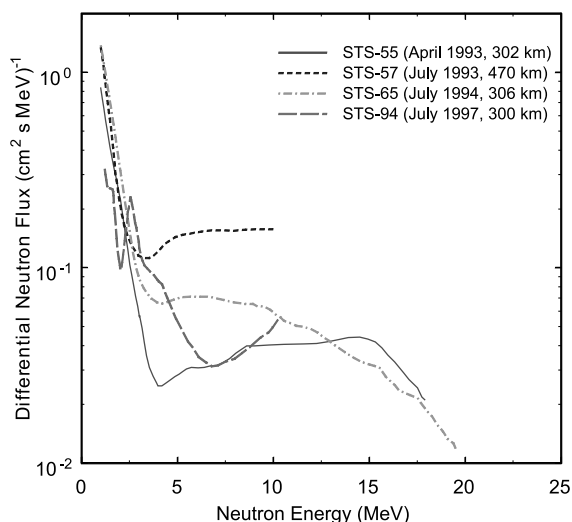


Fig. 28. Differential neutron energy spectra measured by Dudkin using nuclear emulsions aboard four  $28.5^\circ$  Space Shuttle missions [17].

Table 10

Neutron dose and dose equivalent rates measured aboard the Space Shuttle using photographic nuclear emulsions [17]

Shuttle flight	STS-55	STS-57	STS-65	STS-94
Altitude (km)	302	470	306	296
Neutron dose rate ( $\mu\text{Gy/day}$ )	$5.9 \pm 1.4$	$25.3 \pm 6$	$11 \pm 2.7$	$3.7 \pm 0.8$
Neutron dose-equivalent rate ( $\mu\text{Sv/day}$ )	$52.0 \pm 13$	$220 \pm 55$	$95 \pm 23.5$	$30.8 \pm 8$
Mean crew dose rate ( $\mu\text{Gy/day}$ )	57.2	461.9	75.2	101.5
Mean crew dose equivalent rate ( $\mu\text{Sv/day}$ )	120.1	859.4	157.8	213.9
Neutron contribution to dose	10.3%	5.5%	14.6%	3.65%
Neutron contribution to dose equivalent	43.4%	25.6%	60.2%	14.4%

tion to dose-equivalent rate was much greater, varying from 14.4% to 60.2%, and illustrating the important contribution neutrons make to total dose equivalent. It is important to note that this only includes neutrons of energy between 1 and 20 MeV. Neutrons with energy outside this interval, especially higher-energy neutrons in the 100 MeV range, are not included and no accurate measurements of their contribution to total dose equivalent have been made aboard LEO spacecraft.

Neutron energy spectra have been measured aboard the Mir Orbital Station using a number of techniques including photographic nuclear emulsions, activation foils and two active scintillator-based detectors. Fig. 29 shows a total of six neutron energy spectra measured aboard Mir: two spectra measured on the inside of Mir using activation foils, two spectra measured inside Mir using

nuclear emulsion, and two spectra measured on the outside of Mir using scintillator-based neutron spectrometers [53,54]. Also shown in Fig. 29 is a calculation of the neutron energy spectrum predicted for ISS under  $20 \text{ g/cm}^2$  [18]. None of the instruments/methods used to measure the neutron spectrum covered the entire range of neutron energies, although the activation foil measurements came the closest, extending from  $10^{-4}$  to just over  $10^2$  MeV. Above 0.03 MeV, the activation foil measurements are in fairly close agreement with the ISS calculation. Nuclear emulsion measurements extended in neutron energy from  $10^{-2}$  to 10 MeV and over this interval they tend to be in fairly good agreement with the activation foil results. There is exceptionally good agreement between the emulsions and the ISS model calculations between 1 and 10 MeV.

The Granat neutron spectrometer, located on the outside of the Kristal module on Mir, used an organic Stilbene scintillator to measure the neutron energy spectrum between 1 and 14 MeV. Because this spectrometer was mounted outside the spacecraft, it was under significantly less shielding and thus the neutron flux is correspondingly smaller. For this reason it is not appropriate to compare the results from the Granat spectrometer with the model calculations. Fig. 30 shows the neutron spectrum measured by the Granat spectrometer in 1991 under four conditions – inside the SAA, at equatorial latitudes while outside the SAA, at high latitudes and the mean monthly spectrum [53]. The spectrum measured inside the SAA is nearly two orders of magnitude greater than that measured at similar latitudes outside the SAA. The ratio of high-

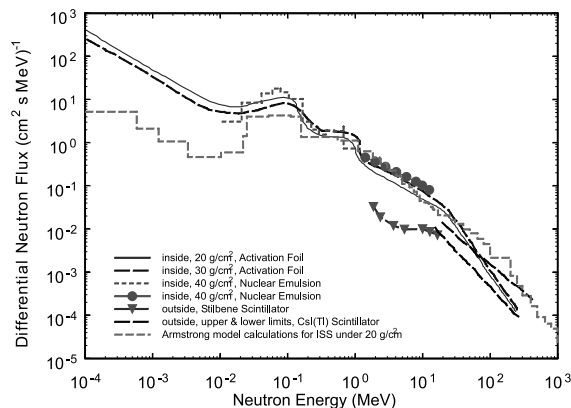


Fig. 29. Neutron energy spectra measured aboard the Mir Orbital Station [53]. Also shown is a model neutron spectrum calculated for the interior of the ISS [18].

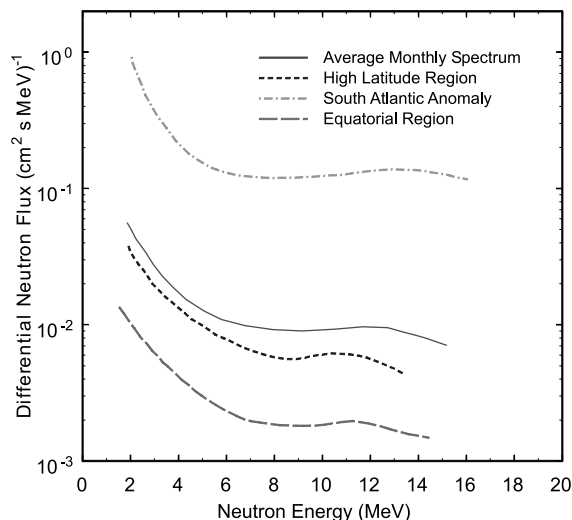


Fig. 30. Neutron energy spectra for four conditions measured by the Granat neutron spectrometer on the outside of the Kristal module on Mir in 1991 [53].

to-low latitude, non-SAA spectra is about 3. This result clearly illustrates that the origin of the vast majority of the neutron flux in this energy interval is from trapped protons in the SAA interacting with the structure and contents of the spacecraft.

### 5.6. Solar particle events

In order for an SPE to significantly enhance the dose rate in LEO, a number of conditions must be met. First, the SPE must possess a large total fluence. The SPE must occur at a longitudinal location on the Sun connected to the Earth via the interplanetary magnetic field so that the particles will arrive at the Earth and not miss it. There must be favorable magnetospheric conditions so that the particles can be transported through the magnetosphere and arrive at LEO, without being first deflected away by the geomagnetic cutoff. Finally the spacecraft has to be in an appropriate orbit. In many cases low-inclination orbits will lie below the geomagnetic cutoff, even if the cutoff latitude is reduced due to the magnetic disturbance associated with the event.

To date, the largest SPE observed on a piloted LEO spacecraft was the October 1989 event as seen

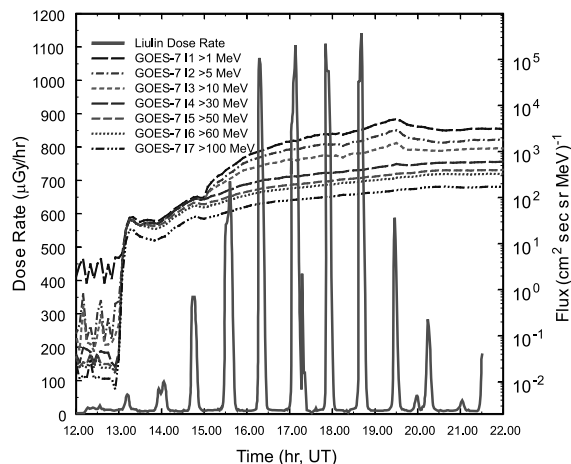


Fig. 31. Dose rate as measured by the Liulin portable spectrometer aboard the Mir Orbital Station during the onset of the 19 October 1989 SPE [33]. Also shown is the differential flux as measured by the NOAA GOES-7 satellite [16].

on Mir. The Liulin portable spectrometer aboard Mir obtained dose rate measurements during the first 12 h of the event [33]. Fig. 31 shows dose rate as a function of time measured by Liulin during the onset of the event [55]. Also shown in Fig. 31 are the GOES-7 proton flux data for the same period [16]. The SPE does not produce a uniform increase in dose rate in LEO as it does in geostationary orbit. Rather elevated dose rate is only encountered when the spacecraft is at high latitudes where the geomagnetic cutoff is sufficiently low to permit the particles to reach LEO. During the October 1989 event, the STS-34 Space Shuttle mission was in a 34.3°, 306 km orbit deploying the Galileo probe to Jupiter. No enhanced dose rate was measured during this mission. By contrast, the R-16 operational dosimeter aboard Mir measured a total of 40 mGy over the course of the September/October 1989 SPEs, an equivalent of about 100 “normal” days exposure aboard Mir [28].

### 5.7. External dosimetry on LEO spacecraft

Experiments to measure dose on the outside of spacecraft as a function of shielding under thin shielding ( $<1 \text{ g/cm}^2$ ) have been carried out on a number of Russian recoverable satellite missions

over the last 20 years by several different research laboratories. Similar experiments have been carried out on the Mir Orbital Station and aboard the US Space Shuttle. These measurements made use of stacks of thin TLDs which were oriented in such a way that the stack was surrounded on all but one side by several  $\text{g/cm}^2$  of shielding [42]. TLDs are stacked on top of each other to a thickness of approximately 1 cm inside an acrylic holder. The loaded acrylic holder is then capped by some thin material such as aluminized Kapton foil. The thickness of Kapton represents the minimum shielding through which the topmost TLD is exposed. Following exposure during the mission and successful recovery, the TLDs are returned to the laboratory and read out using a standard TLD reader. Dose is determined as a function of the position of each TLD within the stack. This position information is then converted to shielding depth in units of  $\text{g/cm}^2$ . Mean dose rate is determined by dividing dose by the duration of the exposure.

Dose rate measured in the thin TLD stacks as a function of shielding depth on the outside of the Mir Orbital Station on two separate occasions is shown in Fig. 32 [42]. The first two measurements were made in June 1991 at a time roughly corresponding to solar maximum. This set of exposures lasted approximately 27 days. The second set of measurements was carried out beginning on 29 April 1997 and ending on 5 September 1997, a period roughly corresponding to solar minimum. Total duration of the second set of exposures was 130 days. The 1991 measurements are approximately one order of magnitude greater than the 1997 measurements over the range of shielding thicknesses measured. In the 1997 measurements, dose rate can be seen to decrease from  $\sim 100$  cGy/day at  $0.01 \text{ g/cm}^2$  to  $\sim 0.1$  cGy/day at  $1 \text{ g/cm}^2$ . On the exterior surface of Mir, the majority of the flux of charged particles take the form of low-energy electrons and protons. Within the first  $\text{g/cm}^2$  of shielding, this low-energy flux is attenuated by nearly three orders of magnitude. Deeper than  $1 \text{ g/cm}^2$  dose rate tends to level off. This is partly due to the fact that shielding from the overhead direction (the TLDs stacked above) is now similar to the shielding from other directions (mostly the sides).

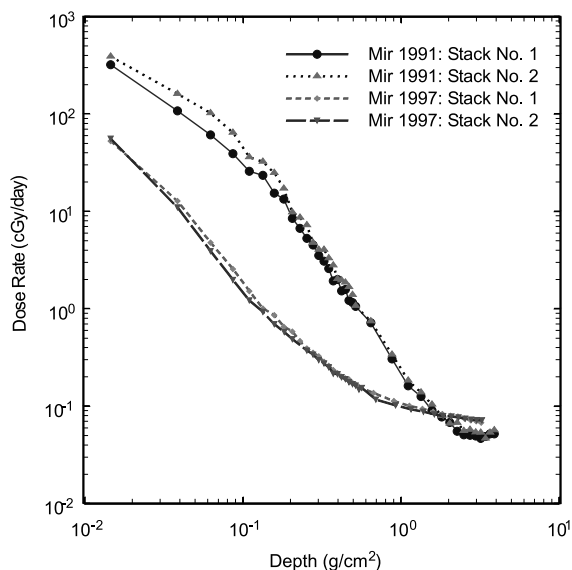


Fig. 32. Dose rate in TLDs as a function of shielding depth measured on the outside of the Mir Orbital Station by the USF group in 1991 and 1997 [42].

Similar measurements have also been made aboard a number of Russian Biocosmos recoverable satellite missions by the Institute of Biomedical Problems, Moscow [56] and the USF group [42], and aboard the US Space Shuttle mission STS-46 (EIOM3 experiment) by the USF group in 1992 [42]. Fig. 33 shows five dose/depth profiles for the different orbital inclinations for which dose/depth information is available. Inclination varied from a near polar orbit of  $82.3^\circ$  to a near equatorial orbit of  $28.5^\circ$ . High-inclination orbits took the Cosmos 1781 ( $70.4^\circ$ ) and Cosmos 2044 ( $82.3^\circ$ ) spacecraft close to the geomagnetic poles, thereby increasing the spacecraft's exposure to the low-energy cusps of the trapped electron belts. This fact is borne out in the higher-dose rates measured at low shielding ( $\sim 0.1 \text{ g/cm}^2$ ) for the high-inclination missions. The low-inclination STS-46 orbit ( $28.5^\circ$ ) avoided the high latitudes. Consequently, the STS-46 curve is the lowest of the five plotted in Fig. 33 and the falloff in dose rate with increasing shielding is not quite as pronounced. Variations in spacecraft altitude and orientation, solar activity, and local shielding environment all probably contribute to differences in the dose/depth profiles measured on the higher-inclination missions.



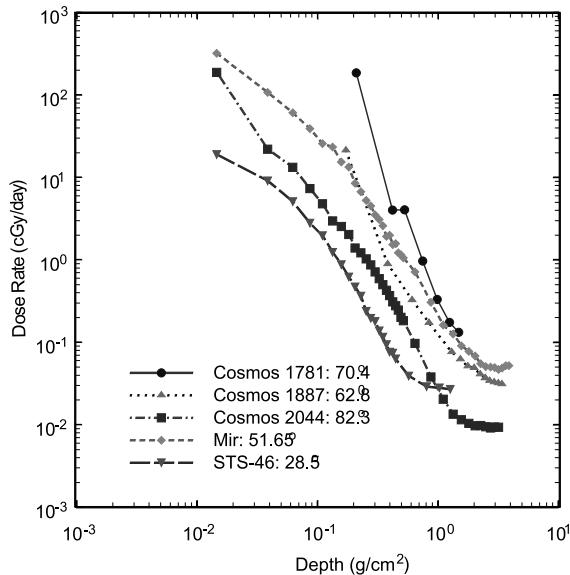


Fig. 33. Dose rate in TLDs as a function of shielding depth measured on the exterior of spacecraft in various inclination orbits by the IMBP [56] and USF groups [42].

To date there has only been one set of dose measurements made during extravehicular activity (EVA). These measurements were made in 1997 during the NASA/Mir Science Program using the Hungarian Pille automatic TLD system [57]. Tables 11 and 12 show the dose and dose rates, respectively, measured by the Pille TLD system by US Astronauts Jerry Linenger and Russian Cosmonaut Vasili Tsebliev during their EVA of 29 April 1997. EVA dose rate is roughly a factor of 4 greater than the dose rate measured on the inside of the Mir when uncorrected for passage through the SAA, and about a factor of 3 greater when corrected for the SAA passage. The Pille TLDs were worn in special pockets on the outside of the

Table 12

Dose rates measured by the Pille TLD system during EVA on 29 April 1997 [57]

Quantity	w/o SAA correction	w/ SAA correction
Dose rate inside ( $\mu\text{Gy/h}$ )	15.5	23.0
Tsebliev dose rate ( $\mu\text{Gy/h}$ )	69.8	77.2
Ratio Tsebliev to inside	4.50	3.35
Linenger dose rate ( $\mu\text{Gy/h}$ )	61.4	68.2
Ratio Linenger to inside	3.96	2.96
Mean EVA dose rate ( $\mu\text{Gy/h}$ )	65.5	72.7
Ratio mean EVA to inside	4.23	3.15

Russian Orlan-M suits and so were less shielded than the bodies of the crew.

## 6. The radiation environment beyond the magnetosphere

The radiation environment outside the Earth's magnetosphere differs markedly from that encountered in LEO. Not only are the trapped radiation belts absent, but interplanetary space lacks the protection afforded by the Earth's magnetic field and the associated geomagnetic cutoff. Due to their high energies, much of the GCR spectrum is highly penetrating. The cost of launching sufficient quantities of shielding is so prohibitive that shielding against GCR during interplanetary spaceflight is out of the question. As described above for LEO, spacecraft shielding can actually serve to increase the mean quality factor of the radiation. Since the energy spectrum associated with SPEs is significantly lower than that for GCR, shielding can play a critical role in reducing crew exposure from SPE in interplanetary space.

Table 11

Doses measured by the Pille TLD system during EVA on 29 April 1997 [57]

Dosimeter	User	Dose ( $\mu\text{Gy}$ )	Dose corrected by internal control ( $\mu\text{Gy}$ )	Dose corrected by internal control and for SAA (Gy)
1A	J. Linenger	415	349	386
2A	V. Tsebliev	373	307	341
4A	Control (inside)	144	—	—

Recently a lot of attention has been paid to possible human exploration of Mars. Minimizing the radiation exposure of the crew both in transit to and from Mars and on the Martian surface is one of the critical constraints driving the planning and design of such missions. In the various scenarios now under consideration, a short, high-speed flight to Mars specifically designed to minimize the radiation exposure of the crew could only be accomplished using some form of nuclear propulsion [58]. However, nuclear propulsion possesses its own inherent source of radiation exposure. A judicious choice in mission timing over the course of the solar cycle can lead to substantial reductions in exposure to GCR due to the dependence of the interplanetary GCR flux on solar modulation (see Fig. 3). Transit to and from Mars during solar maximum, of course, carries with it an increased risk of the occurrence of a major SPE.

Once the astronauts have reached Mars, radiation protection remains an important issue. Exposure to space radiation on the Martian surface is greatly reduced by the shielding provided by the planet itself. In addition, the thin, largely CO<sub>2</sub> atmosphere of Mars provides an additional  $\sim 16$  g/cm<sup>2</sup> of shielding (as compared to 1030 g/cm<sup>2</sup> provided by the Earth's atmosphere at sea level). Mars lacks a strong magnetic field to deflect away lower energy charged particles. Thus, on the Martian surface, exposure to space radiation, while reduced compared to that encountered in free space, is nonetheless omnipresent.

### 6.1. Risks from SPE in interplanetary space

While the geomagnetic field provides significant protection from SPEs to LEO spacecraft, no such protection is available to interplanetary spacecraft flying outside the magnetosphere. During a major SPE proton fluxes aboard spacecraft on trans-Lunar or trans-Martian trajectories would be similar to those measured aboard the geostationary GOES satellites. One of the largest SPEs on record occurred in August 1972, between the Apollo 16 and Apollo 17 Lunar missions. Had an Apollo spacecraft been en route to or from the Moon during this event, the astronauts would

likely have suffered from potentially fatal acute radiation sickness [59].

NASA has carried out a number of studies to model crew radiation exposure during various hypothetical interplanetary and Lunar missions. Several of these studies have focused on the impact of large SPEs [59,60]. A 1996 study by the National Academy of Science's Space Studies Board [61] contained as its first conclusion that "The principle risks of suffering early effects as a result of exposure to radiation in space arise from solar particle events". The risk being addressed here is not carcinogenesis, but acute radiation sickness and related disabilities associated with high fluence, short-term exposure. Such an exposure is associated with the so-called "anomalously large" SPEs, those having fluences of  $>10$  MeV protons in excess of  $10^9$  cm<sup>-2</sup>. Over the last four solar cycles there have been between 2 and 3 such events per solar maximum.

The August 1972 event has often been used as a reference case in predicting SPE doses and dose equivalents to astronauts in interplanetary space. Tables 13 and 14 show the results of a study based on this event carried out by Wilson et al. [60] of the NASA Langley Research Center. Dose and dose equivalent behind polyethylene and aluminum shielding of various thicknesses are calculated for the August 1972 SPE and a "worst case" SPE equivalent to four times the August 1972 event. For a spacesuit (0.4 g/cm<sup>2</sup>) and lightly shielded pressure vessel (1.0 g/cm<sup>2</sup>) estimated doses can exceed the 1.5 Gy considered as a mortality threshold. However, even 5 g/cm<sup>2</sup> of shielding leads to a substantial reduction in dose. The difference between Al and polyethylene shielding is also apparent in Table 13. Because relatively small amounts of shielding can lead to such dramatic decreases in dose, many Mars Transfer Vehicle designs include an SPE "storm shelter".

### 6.2. Free space exposure to GCR

Studies of the GCR exposure of space crews during a Mars mission have tended to focus on issues of shielding composition. Spacecraft have traditionally been constructed out of aluminum, a relatively high *Z* material that enhances the pro-

Table 13

Dose equivalent and dose calculated for critical organs in aluminum and polyethylene structures of four thicknesses during the August 1972 SPE and a hypothetical SPE of four times that of August 1972 [60]

	Space suit (0.4 g/cm <sup>2</sup> )		Pressure vessel (1 g/cm <sup>2</sup> )		Equipment room (5 g/cm <sup>2</sup> )		Shelter (10 g/cm <sup>2</sup> )	
	<i>H</i> (Sv)	<i>D</i> (Gy)	<i>H</i> (Sv)	<i>D</i> (Gy)	<i>H</i> (Sv)	<i>D</i> (Gy)	<i>H</i> (Sv)	<i>D</i> (Gy)
<i>Aluminum structure, August 1972 SPE</i>								
Skin	9.350	4.830	3.560	2.120	0.427	0.294	0.110	0.076
Eyes	3.830	2.400	2.140	1.420	0.367	0.263	0.101	0.071
BFO	0.217	0.157	0.180	0.130	0.065	0.047	0.024	0.017
<i>Polyethylene structure, August 1972 SPE</i>								
Skin	6.770	3.620	2.510	1.540	0.267	0.184	0.058	0.040
Eyes	3.530	2.080	1.810	1.150	0.251	0.171	0.057	0.038
BFO	0.212	0.151	0.174	0.120	0.050	0.034	0.016	0.010
<i>Aluminum structure, 4 × August 1972 SPE</i>								
Skin	374	193	142	85	17	12	4.4	3.0
Eyes	153	96	86	57	15	11	4.0	2.8
BFO	8.7	6.3	7.2	5.2	2.6	1.8	1.0	0.7
<i>Polyethylene structure, 4 × August 1972 SPE</i>								
Skin	271	145	100	62	10.7	7.4	2.3	1.6
Eyes	141	83	72	46	10	6.8	2.3	1.5
BFO	8.5	6.0	7.0	4.8	2.0	1.4	0.6	0.4

Table 14

Expected mortality without adequate medical treatment for four aluminum shielding configurations [60]

Event	Expected mortality (%)			
	Space suit (0.4 g/cm <sup>2</sup> )	Pressure vessel (1 g/cm <sup>2</sup> )	Equipment room (5 g/cm <sup>2</sup> )	Shelter (10 g/cm <sup>2</sup> )
August 1972	1 <sup>a</sup>	1	0	0
1 × August 1972	12 <sup>a</sup>	12	0	0
4 × August 1972	87 <sup>a</sup>	88	3	0

<sup>a</sup> Worst 8 h.

duction of neutrons. Materials rich in hydrogen, such as polyethylene, are a much better choice from the radiation shielding point of view. The shielding properties of a hypothetical, inflatable Mars spacecraft called the TRANSHAB have been investigated using both particle accelerators and computer simulation [62]. Table 15 shows the annual dose equivalent from GCR at 1977 solar minimum for two shielding thicknesses of aluminum, polyethylene, and the TRANSHAB structure calculated by Simonsen et al. [62]. The annual GCR dose equivalent in free space during solar minimum is estimated to be 120 cSv. The dose equivalent is actually higher under 1.51 g/cm<sup>2</sup> of

Table 15

Annual dose-equivalent rates from GCR in free space during solar minimum under two thicknesses of three different shielding materials [62]

Material	1.51 g/cm <sup>2</sup>	5.0 g/cm <sup>2</sup>
Aluminum	130.0 cSv	114.0 cSv
TRANSHAB	120.7 cSv	99.9 cSv
Polyethylene	112.9 cSv	87.0 cSv

The unshielded annual dose equivalent is estimated at 120 cSv.

aluminum than in free space, while it is unchanged and slightly lower for similar thicknesses of the TRANSHAB structure and polyethylene, respec-

tively. Annual solar minimum dose equivalent is lower behind  $5 \text{ g/cm}^2$  of all three materials, but the relative ranking of the three materials in terms of shielding remains unchanged. The development of radiation shielding materials suitable for use in constructing interplanetary spacecraft has recently received much attention within NASA.

Wilson has estimated annual dose equivalents ranging from  $\sim 40$  to  $\sim 140 \text{ cSv}$  under  $1 \text{ g/cm}^2$  Al and ranging from  $\sim 30$  to  $100 \text{ cSv}$  under  $10 \text{ g/cm}^2$  in free space [63]. Simonsen et al. [62] have estimated an annual dose equivalent of  $\sim 9.2 \text{ cSv}$  on the Martian surface. The Mars Reference Mission assumes a 2.5-year total mission duration consisting of a 6-month transit from the Earth to Mars, a 1.5-year stay on the Martian surface, and a 6-month return from Mars to the Earth [58]. For a spacecraft with a mean shielding of  $1 \text{ g/cm}^2$  Al, total dose equivalent for the mission would range between 54 and  $154 \text{ cSv}$ . For a mean shielding of  $10 \text{ g/cm}^2$  Al, the mission dose equivalent would range from 44 to  $114 \text{ cSv}$ .

## 7. Exposure limits for space crews

In the US, the NCRP is responsible for making recommendations on the radiation exposure limits of space crews. The exposure limits currently in use by NASA for LEO were published in NCRP Report No. 98 in 1989 [64]. Recently the NCRP published new recommendations that reduce the whole body limits while leaving the limits to specific organs unchanged [65]. These new recommendations have not yet been adopted by NASA. The Russian career limit is  $4 \text{ Sv}$  with an instantane-

ous limit of  $0.5 \text{ Sv}$  [24]. Currently there are no recommended radiation exposure limits for humans in interplanetary space, although an NCRP committee is currently drafting such recommendations.

The 10-year whole-body radiation exposure limits based on a 3% excess lifetime risk of fatal cancer as recommended by the NCRP in 1989 [64] and 2000 [65] are shown in Table 16. While the older limits are in units of dose equivalent, the new recommendations are in units of equivalent dose, so that the two sets are not strictly intercomparable. Equivalent dose requires both a tissue weighting factor and a radiation weighting factor, the latter being dependent not on LET, but on particle type and energy [66]. Table 17 shows the organ-specific radiation exposure limits as recommended by the NCRP in the 1989 and 2000 reports [64,65]. While the actual limit values have remained unchanged, the units of measure have changed. Like equivalent dose, the determination of gray-equivalent depends on both particle type and energy.

Table 16

Ten year career whole-body limits based on 3% excess lifetime risk of cancer mortality as recommended in NCRP Report 132 (2000) [65] and in NCRP Report 98 (1989) [64]

Age	NCRP-132 equivalent dose E(cSv)		NCRP-98 dose equivalent H(cSv)	
	Female	Male	Female	Male
25	40	70	100	150
35	60	100	175	250
45	90	150	250	325
55	170	300	300	400

Table 17

Organ dose/dose-equivalent limits for all ages and both genders as recommended in [65,64]

	NCRP-132 gray-equivalent (E-cGy)			NCRP-98 dose-equivalent H(cSv)		
	BFO <sup>a</sup>	Eye	Skin	BFO <sup>a</sup>	Eye	Skin
Career	–	400	600	<sup>b</sup>	400	600
Annual	50	200	300	50	200	300
30 days	25	100	150	25	100	150

<sup>a</sup> Blood-forming organ (referred to as bone marrow in NCRP Report 132).

<sup>b</sup> Age dependent, see Table 16.

The limits recommended in Table 16 for LEO are well above the dose equivalents likely to be received by crew members working and living aboard the ISS. Using a mean dose equivalent rate of 650  $\mu\text{Sv/day}$  measured by Benton aboard the Mir Orbital Station near solar minimum [42], a 120-day mission yields a total dose equivalent of 7.8 cSv and a 1-year mission yields a total dose equivalent of 23.7 cSv. It is unlikely that over an astronaut's career, any individual will serve aboard the ISS for a total time in excess of one year. On the other hand, the recommended career limits are of the same order as estimated dose equivalents for a mission to Mars. As mentioned above, these NCRP recommendations are only meant to apply to LEO and further consideration must be taken in establishing limits for human missions to Mars.

## 8. Summary and conclusions

Mean dose rates measured in LEO have tended to be below 500  $\mu\text{Gy/day}$ , regardless of orbital inclination, spacecraft orientation and shielding, and solar cycle phase. The notable exceptions are the high altitude, 28.5° inclination Space Shuttle flights such as the HST servicing missions. On these high-altitude missions, dose rates have routinely been in excess of 2000  $\mu\text{Gy/day}$ . Spacecraft altitude in the SAA is probably the single most sensitive parameter on which dose rate depends.

Exposure to ionizing radiation in LEO is dominated by trapped protons in the SAA. Even in more highly inclined orbits such as the 51.56° orbit of the ISS, roughly half the dose is from SAA trapped protons [2]. Primary trapped protons not only produce a large fraction of the low-LET ( $\leq 10 \text{ keV}/\mu\text{m}$ ) dose, they also are responsible for a significant fraction of the high-LET dose equivalent in the form of target fragments and high-energy neutrons. For interplanetary space travel, trapped protons in the SAA are obviously not a factor.

Historically, major SPEs have not added much to the total doses measured in LEO. This is largely due to the protection afforded by the Earth's magnetic field. The largest SPE observed to date

aboard an LEO spacecraft was the October 1989 event as seen on Mir. The total dose measured aboard Mir by the R-16 operation dosimeter over the course of the September/October 1989 SPE series was 40 mGy – equivalent to about 100 days aboard Mir during quiescent times [28]. For interplanetary spacecraft traveling beyond the protection of the Earth's magnetosphere, SPEs may well represent the single most important radiation risk [61].

The measurement of neutrons aboard spacecraft remains one of the most important unmet challenges facing space radiation dosimetry. Due to the difficulty inherent in neutron dosimetry in a mixed radiation field such as that encountered aboard spacecraft, it is not obvious how to solve this problem. However, those neutron measurements that have been made aboard spacecraft highlight the large contribution secondary neutrons make to the total dose equivalent.

The important effect of shielding in transforming the primary space radiation environment as it passes through a spacecraft has only come to be fully appreciated during the last decade. Prior to this, primary HZE particles were thought to be the major source of high-LET exposure. Radiation surveys conducted aboard spacecraft such as the NASA Space Shuttle and the Mir Orbital Station using instruments such as APDs and the JSC-TEPC have served to illustrate the highly complex effects of spacecraft shielding on dose and dose equivalent rates. The obvious notion that more shielding is better has been shown to be overly simplistic. Modification of the primary radiation field is highly dependent on the specific composition of the shielding material. NASA has recently embarked on several efforts to identify new materials that might be better suited to spacecraft shielding than the traditionally used aluminum.

Most of the space dosimetry data collected to date have been in the form of mean dose rates as measured by TLDs. Although these data are undoubtedly extremely useful, by itself dose is not an adequate quantity by which to assess a person's ionizing radiation exposure. While this is true wherever radiation protection is an issue, it is especially relevant in spaceflight due to the large

number of high-LET particles (both primary GCR and target- and projectile-fragment secondaries) and high-energy neutrons. Technological advances over the past 20 years have led to the development of a number of compact active radiation detectors such as the JSC-TEPC. However, most of these instruments still remain too large and bulky to be used for personal dosimetry. Active portable dosimeters such as Liulin, while providing valuable time-resolved data, are unable to measure the high-LET component. Thus, for the immediate future it appears that passive detectors such as CR-39 PNTDs will remain necessary for monitoring of crew dose equivalent.

The long and productive history of the Mir Orbital Station and the ongoing assembly of the ISS mark the dawn of the permanent human occupation of space. NASA and other organizations are actively studying various scenarios for a return to the Moon and the human exploration of Mars. Larger number of people will soon be spending longer periods of time in space than ever before. As a result, space radiation dosimetry is now more important than at any time in the past and its relevance will only continue to grow. However, it is still too early to consider space radiation dosimetry a mature discipline. Only recently has the importance of neutrons and charged particle secondaries began to be appreciated and our understanding of their contribution to crew exposure is far from complete. NASA has just begun to research ways to minimize crew exposure through the development of shielding-optimized materials out of which to build spacecraft. Although a fair amount of progress has been made in the development of space radiation monitoring instrumentation, an ideal personal dosimeter capable of monitoring the entirety of an astronaut's space radiation exposure, while remaining conveniently compact, is still far away from being a reality. Radiation environment and transport models are in many cases far from perfect. The most significant challenges in space radiation dosimetry are inherent in the complex nature of the space radiation environment itself. Given these considerations, space radiation dosimetry is likely to remain an area rich in opportunity for useful research for a long time to come.

## Acknowledgements

The authors would like to thank Dr. Tony Armstrong of SAIC; Dr. Istvan Apathy and Dr. Sandor Deme of the KFKI Atomic Energy Institute, Budapest, Hungary; Dr. John Wilson of the NASA Langley Research Center, Hampton, VA; Dr. Victor Dudkin of the Research Center for Spacecraft Radiation Safety, Moscow, Russia, and most especially Dr. Gautam Badhwar of NASA Johnson Space Center, Houston, TX for their kindness and generosity in allowing us to reproduce their results.

## References

- [1] J.A. Simpson, in: M.M. Shapiro (Ed.), *Composition and Origin of Cosmic Rays*, NATO ASI Series C: Mathematical and Physical Sciences, Vol. 107, Reidel, Dordrecht, 1983.
- [2] G.D. Badhwar, *Radiat. Res.* 148 (1998) S3.
- [3] J.H. Adams Jr., *NRL Memorandum Report 5901*, Naval Research Laboratory, Washington, DC, 1986.
- [4] G.D. Badhwar, P.M. O'Neill, in: *Proceedings of the 23rd International Cosmic Ray Conference*, Vol. 3, University of Calgary, 1993, p. 535.
- [5] G.D. Badhwar, M.I. Panasyuk, T.I. Pervaya, A.A. Suslov, *Nucl. Tracks Radiat. Meas.* 20 (1992) 427.
- [6] Naval Research Laboratory, CREME96, homepage. <http://crsp3.nrl.navy.mil/creme96/>.
- [7] D. Sawyer, J. Vette, *National Space Science Data Center, Report 76-06*, Greenbelt, MD, 1976.
- [8] J. Vette, *National Space Science Data Center, Report 91-24*, Greenbelt, MD, 1991.
- [9] National Space Sciences Data Center RADBELT model. <http://nssdc.gsfc.nasa.gov/space/model/magnetos/radbelt.html>.
- [10] S.L. Huston, K.A. Pfitzer, *NASA CR-1998-208593*, Marshall Space Flight Center, Huntsville, AL, 1998.
- [11] Time Dependent Radiation-Belt Space Weather Modeling ESTEC Contract No. 11711/95/NL/JG - CCN No. 1 to WO No. 3. <http://www.magnet.oma.be/trend4/public/index.html>.
- [12] Space Environmental Information System (SPENVIS). <http://www.spennis.oma.be/spennis/intro.html>.
- [13] R. Reedy, in: K.S. Balasubramaniam, S.L. Keil, R.N. Smart (Eds.), *Proceedings of the National Solar Observatory/Sacramento Peak 16th International Workshop on Solar Drivers of Interplanetary and Terrestrial Disturbances*, Astronomical Society of the Pacific Conference Series, Vol. 95, 1996.
- [14] R. Turner, *ANSER Technical Report*, Arlington, VA, 1996.

- [15] J.W. Wilson, F.A. Cucinotta, J.L. Shinn, L.C. Simonsen, R.R. Dubbed, W.R. Jordan, T.D. Jones, C.K. Chang, M.Y. Kim, *Radiat. Meas.* 30 (3) (1999) 361.
- [16] NGDC (2001) National Geophysical Data Center on line archive. <http://www.ngdc.noaa.gov/stp/GOES/>.
- [17] G.D. Badhwar, J.E. Keith, T.F. Cleghorn, *Radiat. Meas.* 33 (2001) 235.
- [18] T.W. Armstrong, B.L. Colborn, Science Applications International Corp. Report No. SAIC-TN-9528, 1998.
- [19] F.A. Cucinotta, in: Proceedings of Workshop, Predictions and Measurements of Secondary Neutrons in Space, Houston, TX, 28–30 September 1998.
- [20] J.W. Wilson, F.F. Badavi, F.A. Cucinotta, J.L. Shinn, G.D. Badhwar, HZETRN: Description of a free-space ion and nucleon transport and shielding computer program, NASA TP 3495, Langley Research Center, Hampton, VA, 1995.
- [21] L.W. Townsend, Private communication, 2001.
- [22] L. Pinsky, Private communication, 2001.
- [23] E.R. Benton, A.L. Frank, E.V. Benton, *Radiat. Meas.* 32 (3) (2000) 211.
- [24] E.V. Benton, T.A. Parnell, in: P.D. McCormack, C.E. Swenborg, H. Buckner (Eds.), *Terrestrial Space Radiation and its Biological Effects*, NATO ASI Series A: Life Sciences, Vol. 154, Plenum Press, New York, 1988.
- [25] I. Apathy, S. Deme, L. Bodnar, A. Csoke, I. Hejja, *Radiat. Prot. Dosim.* 85 (1–4) (1999) 321.
- [26] F.D. Badhwar, A. Konradi, W. Atwell, M.J. Golightly, F.A. Cucinotta, J.W. Wilson, V.M. Petrov, I.V. Tchernykh, V.A. Shurshakov, A.P. Lobakov, *Radiat. Meas.* 26 (2) (1996) 147.
- [27] G.D. Badhwar, W. Atwell, B. Cash, M. Weyland, V.M. Petrov, I.V. Tchernykh, Yu.A. Akatov, V.A. Shurshakov, V.V. Arkhangelsky, V.V. Kushin, N.A. Klyachin, E.V. Benton, A.L. Frank, E.R. Benton, L.A. Frigo, D.E. Dudkin, Yu.V. Potapov, N. Vana, W. Schoner, M. Fugger, *Radiat. Meas.* 26 (6) (1996) 901.
- [28] F.G. Mitricas, V.V. Tsetlin, *Radiat. Meas.*, in press.
- [29] F.G. Mitikas, V.V. Tsetlin, *Kosm. Issled.* 33 (4) (1995) 389 (in Russian).
- [30] R. Beaujean, J. Kopp, G. Reitz, *Radiat. Prot. Dosim.* 85 (1–4) (1999) 223.
- [31] T. Sakaguchi, T. Doke, N. Hasebe, T. Hayashi, T. Kashiwagi, J. Kikuchi, S. Kono, S. Nagaoka, T. Nakano, T. Takagi, K. Takahashi, S. Takahashi, *Nucl. Instr. and Meth. A* 437 (1999) 75.
- [32] G.D. Badhwar, J.U. Patel, F.A. Cucinotta, J.W. Wilson, *Radiat. Meas.* 24 (2) (1995) 129.
- [33] Ts.P. Dachev, B.T. Tomov, Yu.N. Matviichuk, R.T. Koleva, J.V. Semkova, V.M. Petrov, V.V. Benghin, Yu.V. Ivanov, V.A. Shurshakov, J.F. Lemaire, *Radiat. Meas.* 30 (1) (1999) 269.
- [34] G.D. Badhwar, Private communication, 1999.
- [35] InterComparison for Cosmic-rays with Heavy Ion Beams At NIRS (ICHHIBAN). <http://www.magnet.oma.be/wrmiss/icchiban/index.html>.
- [36] V. Petrov, Y. Akatov, S. Koslova, V. Markelov, V. Nesterov, V. Redlo, L. Smirenniy, A. Khortsev, I. Tchernykh, *Space Res.* 13 (1975) 129.
- [37] Y.A. Akatov, A.I. Vikhrov, V.E. Dudkin, N.V. Magradze, A.A. Moiseenko, et al., *Cosmic Res.* 23 (1985) 479 (in Russian).
- [38] V.V. Markelov, I.V. Tchernykh, *Radiat. Meas.* 30 (3) (1982) 401.
- [39] Y.I. Vorobyov, Y.Y. Kovalyov, Radiation Safety of Crews of Flying Vehicles, Energoatomizdat, Moscow, 1983 (in Russian).
- [40] G.D. Badhwar, *Radiat. Meas.* 30 (3) (1999) 401.
- [41] G.D. Badhwar, *Health Phys.* 79 (5) (2000) 507.
- [42] E.R. Benton, E.V. Benton, NASA Contractor's Report-1999-209256, Marshall Space Flight Center, AL, 1999.
- [43] G.D. Badhwar, Measurements of Radiation Dose Rates During the NASA-Mir 2 Mission, Internal NASA-JSC Report, 1997.
- [44] G.D. Badhwar, Measurements of Radiation Dose Rates During the NASA-Mir 3 Mission, Internal NASA-JSC Report, 1997.
- [45] W. Schoner, M. Noll, M. Vana, M. Fugger, Yu.A. Akatov, V.A. Shurshakov, in: Proceedings of the 3rd Workshop on Radiation Monitoring for the International Space Station, Budapest, Hungary, 24–26 March 1998.
- [46] G. Reitz, in: Proceedings of the 3rd Workshop on Radiation Monitoring for the International Space Station, Budapest, Hungary, 24–26 March 1998.
- [47] G.D. Badhwar, W. Atwell, E.V. Benton, A.L. Frank, R.P. Keegan, V.E. Dudkin, O.N. Karpov, Yu.V. Potapov, A.B. Akopova, N.V. Magradze, L.V. Malkumyan, Sh.B. Rsh-tuni, *Radiat. Meas.* 24 (3) (1995) 283.
- [48] G.D. Badhwar, M.J. Golightly, A. Konradi, A.W. Atwell, J.W. Kern, B. Cash, E.V. Benton, A.L. Frank, D. Sanner, R.P. Keegan, L.A. Frigo, V.M. Petrov, I.V. Tchernykh, Yu.A. Akatov, V.A. Shurshakov, V.V. Arkhangelsky, V.V. Kushin, N.A. Klyachin, N. Vana, W. Schoner, *Radiat. Meas.* 26 (1) (1996) 7.
- [49] E.V. Benton, A.L. Frank, E.R. Benton, T.W. Armstrong, B.L. Colborn, *Radiat. Meas.* 26 (6) (1996) 799.
- [50] G.D. Badhwar, V.V. Kushin, Yu.A. Akatov, V.A. Mylts-eva, *Radiat. Meas.* 30 (3) (1999) 415.
- [51] E.R. Benton, E.V. Benton, A.L. Frank, *Radiat. Meas.* 33 (2001) 255.
- [52] V.E. Dudkin, Yu.V. Potapov, A.B. Akopova, L.V. Melkumyan, E.V. Benton, A.L. Frank, *Nucl. Tracks Radiat. Meas.* 17 (1990) 87.
- [53] V.I. Lyagushin, V.E. Dudkin, Yu.V. Potapov, V.D. Savastianov, in: Proceedings of Workshop, Predictions and Measurements of Secondary Neutrons in Space, Houston, TX, 28–30 September 1998.
- [54] V.E. Dudkin, Yu.A. Potapov, A.B. Akopova, L.V. Melkumyan, V.G. Bogdanov, V.I. Sacharov, V.A. Plyushev, A.P. Lobakov, V.I. Lyagushin, *Radiat. Meas.* 26 (3) (1996) 535.
- [55] G.D. Badhwar, W. Atwell, *Radiat. Meas.* 30 (3) (1999) 223.
- [56] Yu.A. Akatov, V.V. Arkhangelsky, E.E. Kovalev, F. Spurny, I. Votachkova, *Adv. Space Res.* 9 (1986) 237.

- [57] S. Deme, I. Apathy, I. Hejja, E. Lang, I. Feher, *Radiat. Prot. Dosim.* 85 (1–4) (1999) 121.
- [58] S.J. Hoffman, D.L. Kaplan, NASA Special Publication 6107, Johnson Space Center, Houston, TX, 1997.
- [59] J.W. Wilson, J. Miller, A. Konradi, F.A. Cucinotta (Eds.), *Shielding Strategies for Human Space Exploration*, NASA Conference Publication 3360, Langley Research Center, Hampton, VA, 1997.
- [60] J.W. Wilson, J.L. Shinn, L.C. Simonsen, F.A. Cucinotta, R.R. Dubey, W.R. Jordan, T.D. Jones, C.K. Chang, M.Y. Kim, NASA Technical Paper 3368, Langley Research Center, Hampton, VA, 1997.
- [61] National Academy of Sciences/National Research Council, *Radiation Hazards to Crews of Interplanetary Missions*, National Academy Press, Washington, DC, 1996.
- [62] L.C. Simonsen, J.W. Wilson, M.H. Kim, F.A. Cucinotta, *Health Phys.* 79 (5) (2000) 515.
- [63] J.W. Wilson, *Health Phys.* 79 (5) (2000) 470.
- [64] National Council on Radiation Protection and Measurement, *Guidance on radiation received in space activities*, NCRP Report No. 98, Bethesda, MD, 1989.
- [65] National Council on Radiation Protection and Measurement, *Radiation protection guidance for activities in low-earth orbit*, NCRP Report No. 132, Bethesda, MD, 2000.
- [66] International Commission on Radiological Protection, 1990, *Recommendations of the International Commission on Radiological Protection*, ICRP Report No. 60, Pergamon, Oxford, 1991.